CHALMERS
UNIVERSITY OF TECHNOLOGY

Dynamic Switching Frequency and Advanced Modulation for Automotive Applications

An investigation of efficiency optimization in electric drive lines

Master's thesis in Systems, Control and Mechatronics

Patrik Jönsson
Oscar Dahlin

Department of Electrical Engineering
CHALMERS UNIVERSITY OF TECHNOLOGY
Gothenburg, Sweden 2024
www.chalmers.se

Master's thesis 2024

Dynamic Switching Frequency and Advanced Modulation for Automotive Applications

An investigation of efficiency optimization in electric drive lines

Patrik Jönsson
Oscar Dahlin

CHALMERS
UNIVERSITY OF TECHNOLOGY

Department of Electrical Engineering
Division of Electric Power Engineering
Chalmers University of Technology
Gothenburg, Sweden 2024

Dynamic Switching Frequency and Advanced
Modulation for Automotive Applications
An investigation of efficiency optimization in electric drive lines

Patrik Jönsson
Oscar Dahlin

Supervisor: Tomas Gustafsson, Polestar
Examiner: Torbjörn Thiringer, Division of Electric Power Engineering

Master's Thesis 2024
Department of Electrical Engineering
Division of Electric Power Engineering
Chalmers University of Technology
SE-412 96 Gothenburg
Telephone +46 31 772 1000

Typeset in LaTeX
Printed by Chalmers Reproservice
Gothenburg, Sweden 2024

Dynamic Switching Frequency and Advanced
Modulation for Automotive Applications
An investigation of efficiency optimization in electric drive lines

Patrik Jönsson
Oscar Dahlin

Department of Electrical Engineering
Division of Electric Power Engineering
Chalmers University of Technology

Abstract

The rapid electrification of the vehicle fleets around the world has heavily increased the demand for high efficiency powertrains. The development of this requires thorough evaluation methods for all steps in the power transmission process. One part that can be optimized to increase efficiency is varying the switching frequency in the inverter. Using more complex Pulse Width Modulation (PWM) principles could also be a way to increase efficiency.

In this project, the impact on the electric drive systems efficiency with regard to inverter switching frequency and modulation principle were examined. Also, a simulation model of a real drive system was developed in Matlab, Simulink and JMAG. This model was used to evaluate power losses for different operating conditions of the drive system. The model's results were compared to tests conducted on a physical drive line.

The study showed that a dynamic switching frequency is more power efficient than a fixed one. In terms of PWM principle, the most effective was Space Vector Pulse Width Modulation (SVPWM) for all tested operating conditions. The simulation model's results had a mean difference of 3.5 %-points from the real physical tests.

Keywords: Electric Vehicle, PWM Control, Power Inverter, IPMSM, Efficiency Optimization, Field-oriented Control, Finite Element Method

Acknowledgements

First, we would like to thank the examiner professor Torbjörn Thiringer at Chalmers University of Technology for his knowledge and guidance throughout this work. We would also like to express our gratitude to Tomas Shinkai Gustafsson, Andreas Carlsson, Rasmus Hofswimmer and other employees at Polestar AB for their guidance, support and great answers to the many questions that arose during the conduction of this study.

Patrik Jönsson & Oscar Dahlin, Gothenburg, 2024

List of Acronyms

Below is the list of acronyms that have been used throughout this thesis listed in alphabetical order:

AC	Alternating Current
DC	Direct Current
DPWM	Discontinuous Pulse Width Modulation
EDU	Electric Drive Unit
EMF	ElectroMotive Force
EV	Electric Vehicle
dq	direct-quadrature
FEM	Finite Element Method
FOC	Field Oriented Control
IPMSM	Interior Permanent Magnet Synchronous Machine
MMF	MagnetoMotive Force
MOSFET	Metal Oxide Semiconductor Field Effect Transistor
MTPA	Maximum Torque Per Amplitude
MTPV	Maximum Torque Per Volt
OP	Operating Point
PI	Proportional-Integral
PM	Permanent Magnet
PMSM	Permanent Magnet Synchronous Machine
PWM	Pulse Width Modulation
RMS	Root Mean Square
RPM	Revolutions Per Minute
SPWM	Sinusoidal Pulse Width Modulation
SVPWM	Space Vector Pulse Width Modulation
VSI	Voltage Source Inverter

Contents

1
Introduction

As the automotive industry is rapidly electrifying the vehicle fleets around the world, the demand for higher efficiency in the vehicle's powertrain is increasing. Since the industry is relatively young compared to that of the traditional internal combustion engine, there are still many parts of an electric drive vehicle to examine and improve.

Moreover, the process of evaluating the performance of these components is also rapidly evolving. Having a well developed system for testing and validation is crucial when searching for redundant power consumption in the driveline.

1.1 Problem Background

The Electric Drive Unit (EDU) consists of three main components, being the battery, inverter and electrical machine. The battery is used to store the energy needed for propulsion, which is supplied as Direct Current (DC). The inverter is used to convert and control the DC from the battery to an Alternating Current (AC) of a given frequency and amplitude to be used by the electrical machine, which converts electrical energy to mechanical energy. The power conversion step in the inverter can be optimized in different ways to reduce power losses within the EDU, one being the frequency of which the transistors switch ON and OFF, i.e. switching frequency. The technique used to control the amplitude and fundamental frequency of the output current is done by adjusting the width and shape of the electrical pulses sent to the transistors in the inverter, a technique called Pulse Width Modulation (PWM).

This area is heavily studied in the pursuit of increasing the efficiency of electric vehicles (EV) as there are different sources of energy loss in both the inverter and electrical machine that are affected by the switching frequency and the modulation principle. These include iron and copper losses in the electrical machine, and conduction losses and switching losses in the inverter [1], [2].

A good start for every optimization project is to have a model of the system that can be used to simulate and then evaluate the impact of different parameters and control methods. It is of great interest to create a model which is as accurate to its real world counterpart as possible and to use correct evaluation methods for the model.

1.2 Purpose

The purpose of this project is to investigate the impact on system efficiency concerning inverter switching frequency and modulation strategy, aiming to provide fast and accurate loss estimations that account for PWM effects. In more detail, this project will examine how varying the inverter switching frequency, coupled with PWM techniques, impacts the efficiency of the EDU system. This project aims to investigate the influence of different modulation strategies, such as Space Vector Pulse Width Modulation (SVPWM) and Discontinuous Pulse Width Modulation (DPWM), on the losses in the EDU system. Additionally, it seeks to evaluate the extent to which simulation results align with experimental data obtained from physical EDU tests, specifically regarding the effects of PWM.

2
Theory

2.1 Inverter

In Figure 2.1 a conventional three phase two-level Voltage Source Inverter (VSI) is illustrated. The primary function is to convert DC to three-phase AC for e.g. an electrical machine.

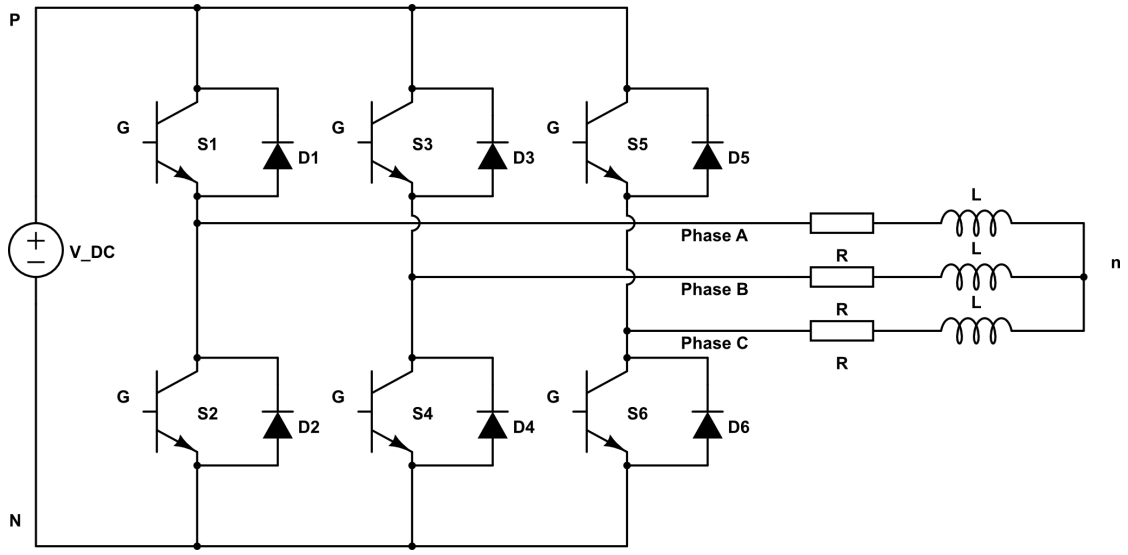

Figure 2.1: Three-phase two-level VSI.

The three-phase inverter consists of six transistors, also known as switches, where transistors S_1 and S_2 creates the first leg, S_3 and S_4 the second leg and S_5 together with S_6 creates the third leg. Each leg generates one of three phases supplied to a load. At any time instant in a leg, only one switch is in conduction state (1, ON) and the other one is non-conducting state (0, OFF). By switching these transistors ON and OFF through different modulation principles the AC voltage can be synthesized. These ON and OFF time intervals for each transistor pair is determined from the PWM strategy used. The different strategies eventually produces PWM signals in the form of square waves that controls the switching of the transistors. These square waves are also called gate signals, denoted G in Figure 2.1.

In Table 2.1 the eight possible switch states for the inverter are depicted with their corresponding output voltage [3]. V_{AB}, V_{BC} and V_{CA} are the line-to-line voltages, V_{An}, V_{Bn} and V_{Cn} are the phase-to-neutral voltages [V]. V_{DC} [V] is the DC link voltage supplied by the voltage source, e.g. a battery. The neutral is depicted with "n" in Figure 2.1.

Table 2.1: Inverter switch-states and output voltages

S1	S3	S5	V_{AB}	V_{BC}	V_{CA}	V_{An}	V_{Bn}	V_{Cn}
1	1	1	0	0	0	0	0	0
0	1	1	-V_{DC}	0	V_{DC}	-$\frac{2}{3}$ V_{DC}	$\frac{1}{3}$ V_{DC}	$\frac{1}{3}$ V_{DC}
1	0	1	V_{DC}	-V_{DC}	0	$\frac{1}{3}$ V_{DC}	-$\frac{2}{3}$ V_{DC}	$\frac{1}{3}$ V_{DC}
1	1	0	0	V_{DC}	-V_{DC}	$\frac{1}{3}$ V_{DC}	$\frac{1}{3}$ V_{DC}	-$\frac{2}{3}$ V_{DC}
0	0	1	0	-V_{DC}	V_{DC}	-$\frac{1}{3}$ V_{DC}	-$\frac{1}{3}$ V_{DC}	$\frac{2}{3}$ V_{DC}
1	0	0	V_{DC}	0	-V_{DC}	$\frac{2}{3}$ V_{DC}	-$\frac{1}{3}$ V_{DC}	-$\frac{1}{3}$ V_{DC}
0	1	0	-V_{DC}	V_{DC}	0	-$\frac{1}{3}$ V_{DC}	$\frac{2}{3}$ V_{DC}	-$\frac{1}{3}$ V_{DC}
0	0	0	0	0	0	0	0	0

Only the high side transistors are used to describe the switching states since the lower ones are the negation of the upper ones. For state (S1, S3, S5) = (1, 0, 0) for example, phase A to neutral voltage (V_{An}) = $\frac{2}{3}V_{DC}$, $V_{Bn} = \frac{-1}{3}V_{DC}$ and $V_{Cn} = \frac{-1}{3}V_{DC}$ which can be seen in Table 2.1. Then the current for phase A flows through S1 and then through the load whereas for phase B and C the current flows from the neutral through S4 and S6 respectively. If both transistors in a leg would be turned ON at the same time, the battery would be short-circuited. To remove the risk of this, the length of the square waves (gate signals) are reduced by a short time interval ($\approx$ 1 µs), also called blanking-time [4]. During this time, both transistors in a phase leg are in their non-conducting state. Therefore the anti-parallel diodes (D1 - D6) in Figure 2.1 are needed to provide a path for the current to flow when the upper and lower transistor in the same phase leg are turned OFF (blanking-time).

However, this blanking-time introduces a voltage error between the desired voltage suggested by the PWM and the actual voltage out from the inverter since neither of the transistors in the phase leg conducts current. This error is proportional to the ratio between the blanking time and switch period and can be mitigated by adding a signal to the modulation waves [4]. It can be calculated by the voltage drop induced from the diode when it conducts current and the ratio between blanking-time and the switching period as

$$u^* = sgn(i_x)\left(\frac{t_{blank}}{T_{sw}} + \frac{V_{diode}(|i_x|)}{V_{DC}}\right) \tag{2.1}$$

where:

- i_x is the current through the diode for phase A, B or C [A]
- t_{blank} is the blanking time [s]
- T_{sw} is the switching period [s]
- V_{diode} is the voltage drop of the diode [V]

2.2 PWM Principles

There are different methods for creating the PWM waves that controls the switching of the transistors in the inverter. Such methods are called modulation principles and these concepts will be explained in this chapter.

2.2.1 Sinusoidal Pulse Width Modulation (SPWM)

Figure 2.2 showcases the basic principle of the SPWM modulation principle. There is a carrier wave (usually a triangular signal) and three reference signals (sinusoidals), one for each phase. The carrier wave's frequency is usually much higher relative to the frequency of the reference signals.

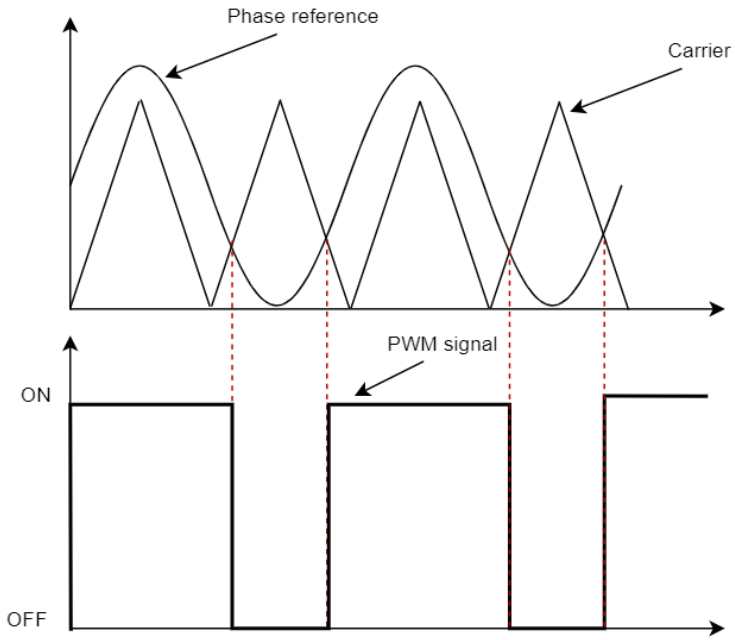

Figure 2.2: Single-phase SPWM.

The carrier wave is compared with all reference signals which are 120° shifted apart. When the reference phase voltage is larger than the carrier wave, then the upper switch in that particular leg for that phase is turned ON, and the lower one is turned OFF. Hence, the current flows through the upper switch and through the load. The same principle goes for the other legs as well. In that way these PWM square wave signals are generated which controls the switching states of the inverter to mimic the reference sinusoidals being used. For SPWM the maximum amplitude of the fundamental phase voltage is [5]

$$V_{max} = \frac{V_{DC}}{2} = 0.5\ V_{DC} \tag{2.2}$$

where V_{max} [V] is the maximum line-to-neutral output voltage that the inverter can produce.

2.2.2 Space Vector Pulse Width Modulation (SVPWM)

SVPWM is a modulation technique where only one transistor is operating at a time, but still, the idea is that a reference voltage is transformed into switching signals for the inverter. However, this modulation technique operates in the $\alpha\beta$-frame (see section 2.4.1) instead of the ABC-frame as the SPWM does [4]. Because of the inverter nature, there are eight possible switching states, or base vectors as they are referred to. These switching states can be represented binary by considering the transistor pair for each phase (A, B and C). When the switching state (A, B, C) = (1, 0, 0), it yields that in the phase A leg, the upper switch is ON and hence conducting, and the upper switches for B and C are OFF (thereby the lower ones are ON and conducting). In Figure 2.3 these base vectors corresponding to the eight possible switching states are depicted together with their binary representations in the $\alpha\beta$-frame. The phase voltages (120°apart) in the ABC-frame are also visualized.

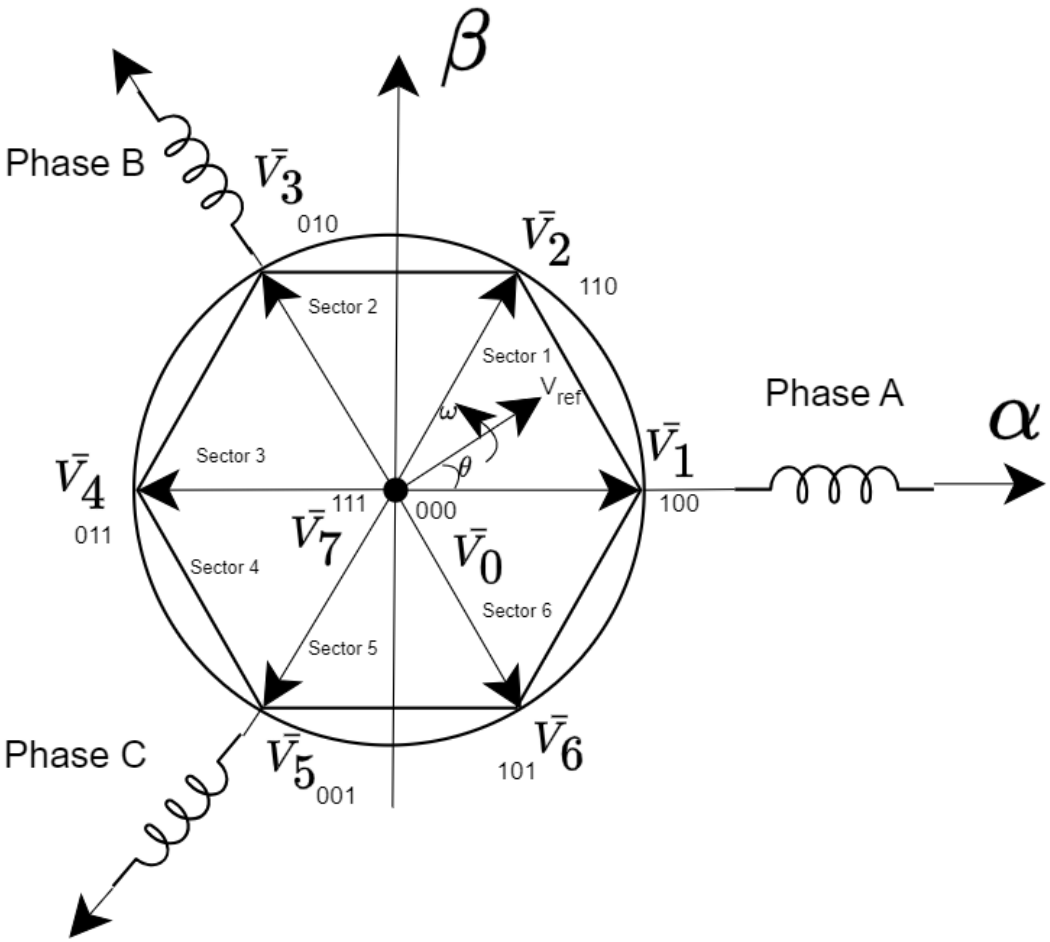

Figure 2.3: SVPWM base vectors in the $\alpha\beta$-frame.

The switching states when either all upper or all lower transistors are in conducting state (zero-sequence state), are located in the origin since these make the output voltage equal to zero since they are short-circuiting lower or upper set of switches [6]. Apart from these the base vectors that are non-zero are located in the edges of the hexagon. The operation principle is as follows; the desired sinusoidal (reference phase voltage) for each phase can be represented in this figure. At each time instant they will be located in one of these six sectors. For example, it could be located between vector $\bar{V_1}$ and $\bar{V_2}$ in sector 1 as depicted by V_{ref} in Figure 2.3. To synthesize this reference phase voltage the switching pattern can be alternated between the binary representations 100, 110 and the null vectors, where each state is active for a different amount of time. To clarify, the reference phase voltage can thereby be represented as

$$V_{ref} = \bar{V_1}T_1 + \bar{V_2}T_2 + \bar{V_0}T_0 \tag{2.3}$$

where T_0, T_1 and T_2 [s] are the duration that the corresponding space vector is ON. Therefore, the reference phase voltage for each sector can be created by being in each switching state in that particular sector for a certain amount of time. The advantage of this method is that less commutations (changes of the switch states) are needed within each PWM period due to the zero-sequence signal injection technique [4]. Since each ON and OFF switch in a transistor is associated with energy loss, the SVPWM method increases the efficiency of the inverter as compared to the SPWM. This is due to the fact that SPWM considers each phase independently which leads to more commutations and in turn more energy loss during the same time period.

For SVPWM the maximum amplitude of the fundamental phase voltage is [5]

$$V_{max} = \frac{V_{DC}}{\sqrt{3}} \approx 0.577\ V_{DC} \tag{2.4}$$

In fact, the utilization of the DC link voltage in SVPWM is 15.5% larger than for SPWM since SPWM only utilizes 86.6% of the DC voltage U_{DC} [7].

SVPWM can be implemented in an inverter by using SPWM and injecting the min/max value of a triangular wave to the sinusoidal reference wave. The resulting modulation wave in Figure 2.4, when compared to the carrier wave, will turn the switches ON and OFF according to the sector sequence discussed above.

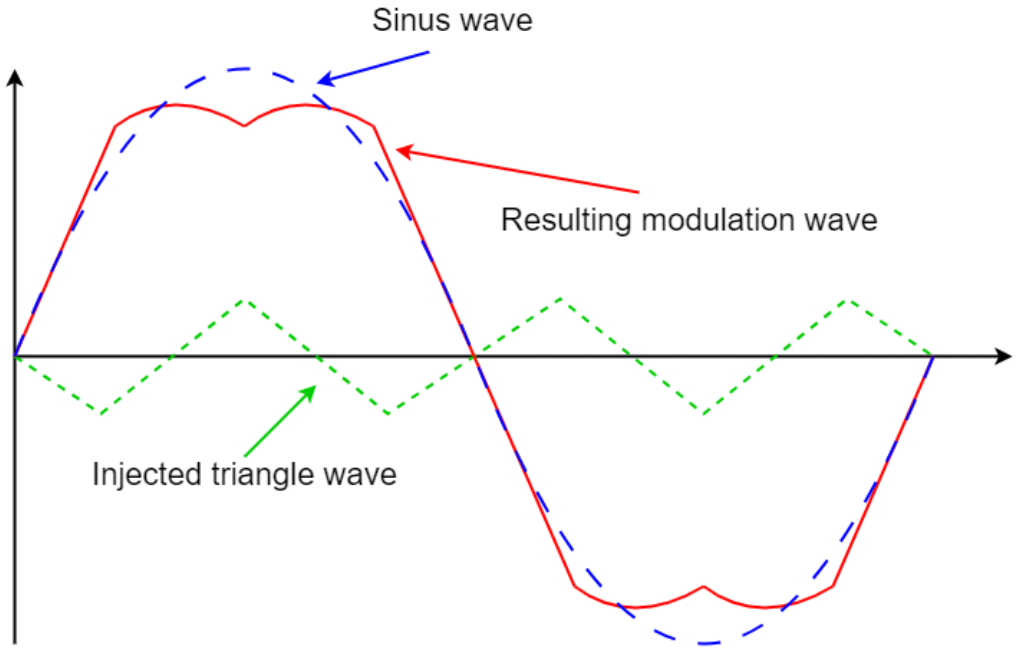

Figure 2.4: Modulation wave for SVPWM.

2.2.3 Discontinuous Pulse Width Modulation (DPWM)

In the DPWM technique the basic principle is that the reference phase voltages are modulated by injecting zero-voltage intervals for a certain amount of time during each PWM period. Therefore, during each PWM period one of the phases is not switching, such that the output voltage for that phase is clamped to the positive or negative DC link voltage by having high or low transistor constantly on, making one of the phases to cease modulation. Hence, the switching losses in that inverter leg are removed during that PWM period. Figure 2.5 visualizes how the modulated reference (orange curve) looks together with the original phase reference (black dashed curve) and the zero-sequence signal (green dotted curve). From there one can see that when taking the original phase voltage reference sinusoidal wave and adding the zero-sequence signal, the DPWM reference wave is created.

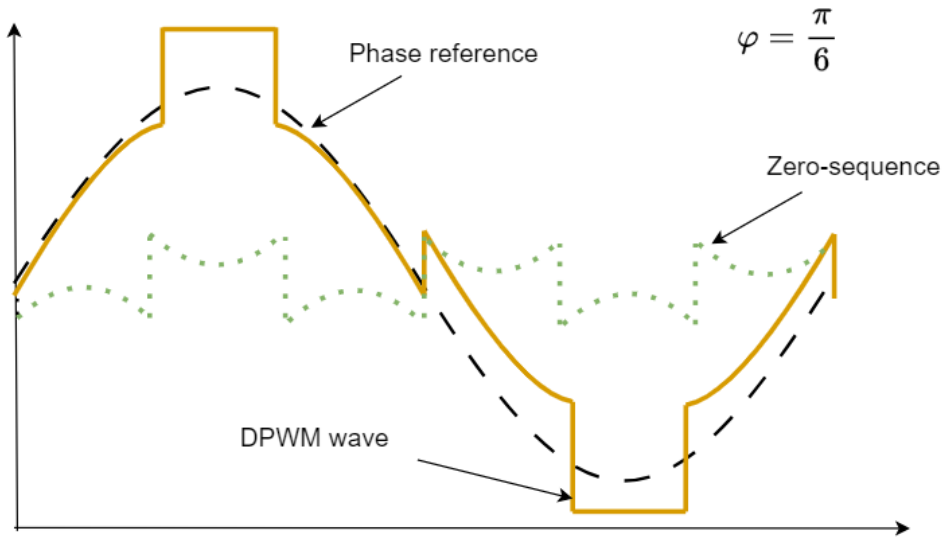

Figure 2.5: DPWM wave with the zero-sequence signal and the phase reference for $\varphi = \frac{\pi}{6}$ [rad] phase shift.

In the DPWM method different modulator phase angles (φ) can be used which determines the angle shift between the DPWM wave in relation to the initial sinusoidal reference. In Figure 2.5 a phase shift of $\frac{\pi}{6}$ [rad] (30°) is used but other phase shifts can be used to create different DPWM principles with other behaviors. Moreover, the duration of the clamped modulation wave to the DC link voltage is a design parameter that can be used to tune the control of the inverter. The DPWM principle has a superior voltage linearity range, reduced switching losses and superior high modulation range current waveform quality but poor low modulation range performance in terms of narrow pulse problems and poor current waveform quality [8]. The utilization of the DC link voltage for DPWM can be expressed as

$$V_{max} = \frac{2V_{DC}}{\pi} \approx 0.637\ V_{DC} \tag{2.5}$$

where V_{max} is the maximum line-to-neutral output voltage that the inverter can produce [8].

2.3 Inverter Power Losses

The inverter, which operates in a switching mode through PWM techniques, is prone to power losses in the transistors as well as the diodes. These power losses, P_{inv} [W], can be modelled as

$$P_{inv} \approx P_c + P_{sw} \tag{2.6}$$

when neglecting the blocking leakage losses, an insignificantly small loss that occurs in transistors that are in their OFF state but still leaks very small current. Here P_c [W] and P_{sw} [W] are the conduction losses and switching losses respectively [9].

2.3.1 Conduction Losses

When the components in the inverter, such as diodes and transistors, conduct current they dissipate power as heat since the current flows through a resistive element. The conduction losses of the Metal Oxide Semiconductor Field Effect Transistor (MOSFET) can be approximated by the resistance between drain-source in the ON-state $R_{DS,ON}$ [Ω]. The voltage drop over the MOSFET:s can be calculated as a function of the drain current I_{DS} [A] as

$$U_{DS}(I_{DS}) = R_{DS,ON}(I_{DS})I_{DS} \tag{2.7}$$

where $U_{DS}(I_{DS})$ [V] is the voltage across the drain and source as a function of the drain current. Hence, the instantaneous ($P_{c,mos,ins}$ [W]) and average ($P_{c,mos,avg}$ [W]) conduction loss in the MOSFET:s are given by

$$P_{c,mos,ins} = U_{DS}(t)I_{DS}(t) = R_{DS,on}I_{DS}^2(t) \tag{2.8a}$$

$$P_{c,mos,avg} = \frac{1}{T_{sw}}\int_0^{T_{sw}} P_{c,mos,ins}dt = \frac{1}{T_{sw}}\int_0^{T_{sw}} R_{DS,on}I_{DS}^2(t)dt = R_{DS,on}I_{DS,rms}^2 \tag{2.8b}$$

where T_{sw} [s] is the time duration of the switching cycle and $I_{DS,rms}$ [A] is the root mean square (RMS) value of the MOSFET:s ON-state current [9].

Furthermore, the anti-parallel diode also contributes to the conduction losses. By utilizing a diode approximation cascade connected to a DC voltage source U_{D0} [V], which represents the diode ON-state zero-current voltage, this conduction loss can be estimated as

$$U_D(I_D) = U_{D0} + R_D I_D \tag{2.9}$$

where R_D [Ω] is the diode ON-state resistance, U_D [V] is the voltage across the diode and I_D [A] is the current through the diode.

The instantaneous diode conduction loss ($P_{c,dio,ins}$ [W]) and the diode conduction loss across the switching period ($P_{c,dio,avg}$ [W]) can then be calculated respectively by

$$P_{c,dio,ins} = U_D(t)I_D(t) = U_{D0}I_D(t) + R_D I_D^2(t) \tag{2.10a}$$

$$P_{c,dio,avg} = \frac{1}{T_{sw}} \int_0^{T_{sw}} P_{c,dio,ins}(t)dt = \frac{1}{T_{sw}} \int_0^{T_{sw}} (U_{D0}I_D(t) + R_D I_D^2(t))dt = \\ = U_{D0}I_{D,avg} + R_D I_{D,rms}^2 \tag{2.10b}$$

where $I_{D,avg}$ [A] is the average current through the diode and $I_{D,rms}$ [A] is the RMS value of the diode current [9].

2.3.2 Switching Losses

Switching losses occur in the transistors of the inverter during the time when the transistor transitions between the ON and OFF states. During this period, the transistor is in a region where both its current and voltage is changing at the same time, resulting in energy losses [1]. The switching loss for the MOSFET, $P_{M,sw}$ [W], can be calculated as

$$P_{M,sw} = \frac{\sum E_{M,sw}}{t} \tag{2.11}$$

where the energy consumed by each ON and OFF switch is denoted $E_{M,sw}$ [J] and can be obtained from data sheet information. The energy for each ON and OFF switch is summed to the total amount of switches and then divided by the total duration time t [s] [10].

The anti-parallel diodes in the inverter are also prone to switching losses. These switching losses ($P_{D,sw}$ [W]) can be expressed by

$$P_{D,sw} = (E_{D,on} + E_{D,off})f_{sw} \approx E_{D,on}f_{sw} = \frac{\sum E_{D,on}}{t} \tag{2.12}$$

where f_{sw} [Hz] is the switching frequency. Moreover, $E_{D,on}$ [J] is the reverse recovery energy for the anti-parallel diode (occurred when the parallel transistor turns ON) and $E_{D,off}$ [J] is the energy when the anti-parallel diode conducts current (occurred when the parallel transistor turns OFF) [9]. The reverse recovery process of the diode is present when the diode switches from the conducting state to the non-conducting state. This process takes some time, depending on the diodes used, during which power is lost due to the removal of stored charge carriers within the diode.

2.4 Electrical Machine

Electrical machine is a term for a device that transforms electrical energy to mechanical energy with the use of magnetic fields [11]. Electrical machines can be divided into three categories, AC Synchronous motors, AC Asynchronous motors and DC motors [12]. This thesis will be conducted on an AC Synchronous motor, more precisely a Permanent Magnet Synchronous Machine (PMSM), as it is the most commonly used type in Electric Vehicles (EV:s) [13].

2.4.1 Space Vector Transformation

The use of three-phase AC in a PMSM leads to complicated calculations for the control of the machine due to the rotating dynamics of the rotor shaft. This can be simplified with the following equation

$$\begin{bmatrix} x_\alpha \\ x_\beta \end{bmatrix} = K \begin{bmatrix} \frac{2}{3} & -\frac{1}{3} & -\frac{1}{3} \\ 0 & \frac{1}{\sqrt{3}} & -\frac{1}{\sqrt{3}} \end{bmatrix} \begin{bmatrix} x_a \\ x_b \\ x_c \end{bmatrix} \tag{2.13}$$

which is called the Clarke transformation [14]. It transforms the space vectors x_a, x_b and x_c of the currents or voltages in the 3-phase coordinate system, to the space vectors x_α and x_β in the 2-dimensional, orthogonal alpha-beta ($\alpha\beta$-) coordinate system. This transformation from three-phase to two-phase can be done without losing any information if there is no zero-sequence (i.e. if all phases adds to zero at all time instances). The constant K is used for scaling and can be selected arbitrarily, $K \neq 0$. To further simplify the calculations for a rotating system, the x_α and x_β can be transformed using

$$\begin{bmatrix} x_d \\ x_q \end{bmatrix} = \begin{bmatrix} cos(\theta_r) & sin(\theta_r) \\ sin(\theta_r) & cos(\theta_r) \end{bmatrix} \begin{bmatrix} x_\alpha \\ x_\beta \end{bmatrix} \tag{2.14}$$

also called the Park transformation [14]. Here x_d and x_q are perpendicular space vectors in the direct-quadrature (dq-) coordinate system and θ_r [rad] is the electrical rotor position (angle from the α-axis to the rotating d-axis). The d-axis is aligned in the same direction as the rotors magnetic flux (Field Oriented Control (FOC)) and the q-axis is aligned to the rotors electric field, which makes this coordinate system rotate with the same angular frequency as the rotor. In Figure 2.6 the effect of the transformations made from (2.13) and (2.14) can be seen visually.

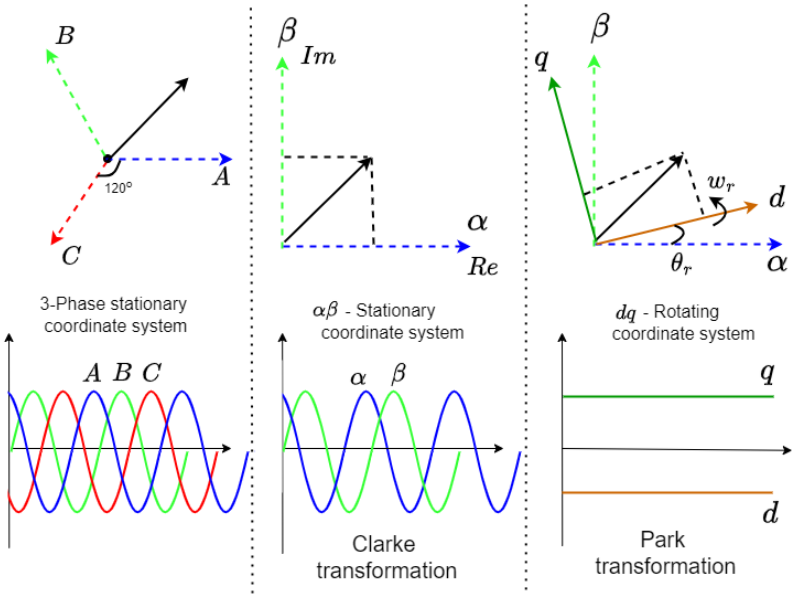

Figure 2.6: Coordinate systems and transformations.

Noticeable in Figure 2.6 is that the Park transformation converts AC quantities to DC quantities since the coordinate system rotates along with the rotor.

2.4.2 Structure

The machine consists of a rotor and stator. The rotor is a rotating part connected to the load through a rigid shaft. For a PMSM, the stator consists of a laminated iron core with insulated coils inside arranged in a circular pattern outside the rotor's magnets. The coils are fed by a three-phase AC which induces a rotating magnetic field, that in turn creates a torque on the rotor when the Permanent Magnets (PM:s) in the rotor are forced to align with the rotating magnetic field produced by the stator winding [11].

A PMSM can have its magnets attached to the rotor in different configurations, in this thesis an Interior mounted PMSM (IPMSM), where the PM:s are moulded into to the rotor, will be used. For an IPMSM the inductance along the q-axis is greater than the inductance along the d-axis ($L_d < L_q$ [H]) which enables it to utilize both magnetic and reluctance torque [15]. Since the magnets are moulded into the laminate, the machine gets a higher torque since the surrounding iron laminate has a higher magnetic permeability than air. A schematic of the general structure is shown in Figure 2.7 alongside with the stator currents (A, B and C) and the resulting magnetic flux densities (B_A, B_B and B_C [T]) generated by the stator currents.

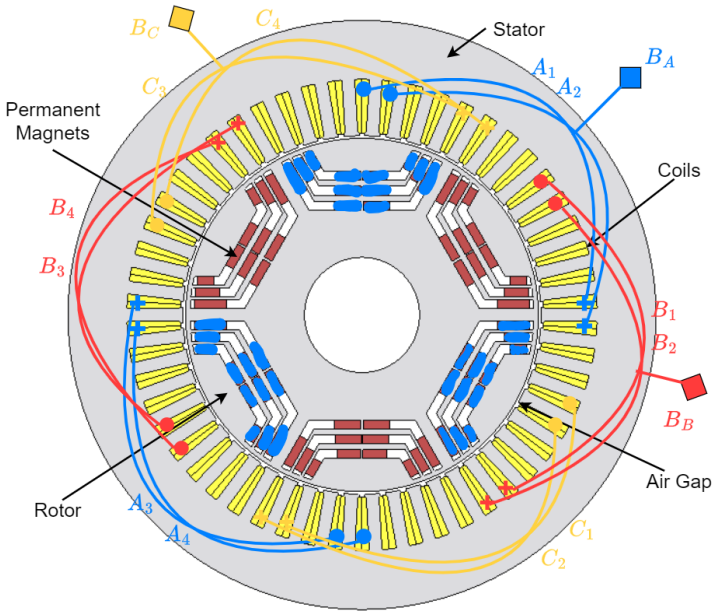

Figure 2.7: Generic 2D IPMSM model with 56 slots, 3 pole-pairs and distributed winding with stator currents A, B and C drawn together with the resulting magnetic flux density for each phase.

In Figure 2.7 the PM:s are mounted in the rotor which generates a magnetic field inside the electrical machine. The red PM:s are the north-poles and the blue PM:s are the south-poles, therefore it is in total 6 poles in the rotor which corresponds to 3 pole-pairs. There are also 56 slots, or stator teeth, which are the grey area in between the yellow sections. They have coated copper wires wound around them in order to generate the magnetic flux. The wires are coated to prevent a short-circuit by isolating them from each other. The winding sketched are called distributed winding, where each phase is wound around a number of slots. Moreover, this configuration has 2 stator pole-pairs which comes from the fact that for each phase there are two winding placed opposite of each other where each winding creates a pole-pair. In fact, the number of pole-pairs generated in the rotor from the PM:s should match the number of pole-pairs in the stator winding, but in Figure 2.7 some has been excluded to make the figure clearer for illustrative purposes.

The direction of the magnetic flux generated by the current in the winding can be determined by using Amperes right-hand rule. The flux direction generated by the first and second winding for phase A (A_1 and A_2) in Figure 2.7 is labeled B_A, the same goes for the other phases. By putting the fingers in the direction of the current, the thumb points in the direction of the magnetic flux. In Figure 2.7 the direction of the current is depicted with "X" and "O" symbols, "X" means that the current goes in to the "X" and "O" that the current comes out from the "O". In summary, there are two individual magnetic fields produced. One generated by the PM:s in the rotor and the other from the 3-phase AC flowing through the stator coils. In steady-state these magnetic fields aligns with each other and rotates synchronously, achieving synchronous speed.

2.4.3 Faraday's Law of Induction

Faraday's law of induction describes how a changing magnetic field induces an ElectroMotive Force (EMF) in a circuit. Physically it states that the magnitude of the EMF induced in a circuit is proportional to the rate of change of the magnetic flux and can be written as [16]

$$\mathscr{E} = -\frac{d\Phi}{dt} \tag{2.15}$$

where:

- $\mathscr{E}$ is the EMF [V]
- Φ is the magnetic flux [Wb]

An EMF is a voltage that arises in a conductor either from conductors moving in a magnetic field or from a changing magnetic field [16]. The negative sign in (2.15) originates from Lenz's law which proposes that the direction of an induced current, by a changing magnetic field, is such that it opposes the change of flux that induced it.

2.4.4 IPMSM Related Magnetic Theory

As mentioned in section 2.4.2 the AC flowing in the stator coils for the three phases induces a magnetic field. The emergence of this magnetic field is Faraday's law of induction as described in section 2.4.3. The magnetic flux generated by the three-phase AC in the stator can be related to the magnetic field density through (2.16)

$$\Phi = \int\int_s Bds \propto AB \tag{2.16}$$

where:

- A is the area that the magnetic field density flows through [m^2]
- B is the magnetic flux density [T]

When having coils as in Figure 2.7 it is convenient to introduce the term flux linkage which is defined as the product between the magnetic flux and the number of turns in the winding as

$$\Psi = N\Phi \tag{2.17}$$

where:

- N is the number of turns in the coil [-]
- Ψ is the flux linkage [Wb]

The enclosed loop of magnetic field strength is also known as the MagnetoMotive Force (MMF) and can be calculated with Ampere's law on integral form stated in (2.18)

$$\mathscr{F} = \oint_l H dl = I_{encl} = Ni(t) \tag{2.18}$$

where:

- $\mathscr{F}$ is the MMF [A_{turn}]
- H is the magnetic field intensity [A/m]
- l is the length of the circumference of the enclosed area [m]
- I_{encl} is the current flowing through the enclosed area [A]
- i(t) is the conductor current [A]

MMF can be generated by having a current flow through a coil and it is the phenomena giving rise to magnetic fields. For PM:s as in the rotor of the IPMSM used in this thesis the MMF can be calculated as [17]

$$\mathscr{F} = H_{mag} t_{mag} \tag{2.19}$$

where t_{mag} [m] is the thickness of the magnet in the direction of the magnet polarization. The MMF, for both coil excitation (2.18) and PM excitation (2.19), creates a magnetic flux which size is dependent on the reluctance and can be calculated by Hopkinson's law defined in (2.20)

$$\mathscr{F} = \Phi \mathscr{R} \tag{2.20}$$

where:

- $\mathscr{R}$ is the reluctance [H^{-1}]

Reluctance is the level of difficulty experienced by a magnetic flux to flow in a magnetic circuit and can be calculated as [17]

$$\mathscr{R} = \frac{l}{\mu_0 \mu_r A} \tag{2.21}$$

where:

- μ_0 is the permeability in vacuum [H/m]
- μ_r is the relative permeability of the material [-]

In a IPMSM iron is used because it has a high relative permeability which implies that it can easily be magnetized. Hence stronger magnetic fields are created more efficiently which is desirable.

The above mentioned magnetic properties and phenomena can be closely related to the concept of electrical circuits. The analogy to make here is that the MMF is correspondent to the voltage in an electrical circuit. In the same way as voltage is needed to make current flow, the MMF is what gives rise to magnetic flux in magnetic circuit. The same goes for the analogy between resistance in an electrical circuit and reluctance in a magnetic circuit, in regards that the reluctance is a measure of opposition in magnetic flux.

2.4.5 Dynamic Model

Equations (2.13) and (2.14) enable a representation of the electrical machine with DC dynamics instead. The equivalent circuit of the model in dq-frame is shown in Figure 2.8.

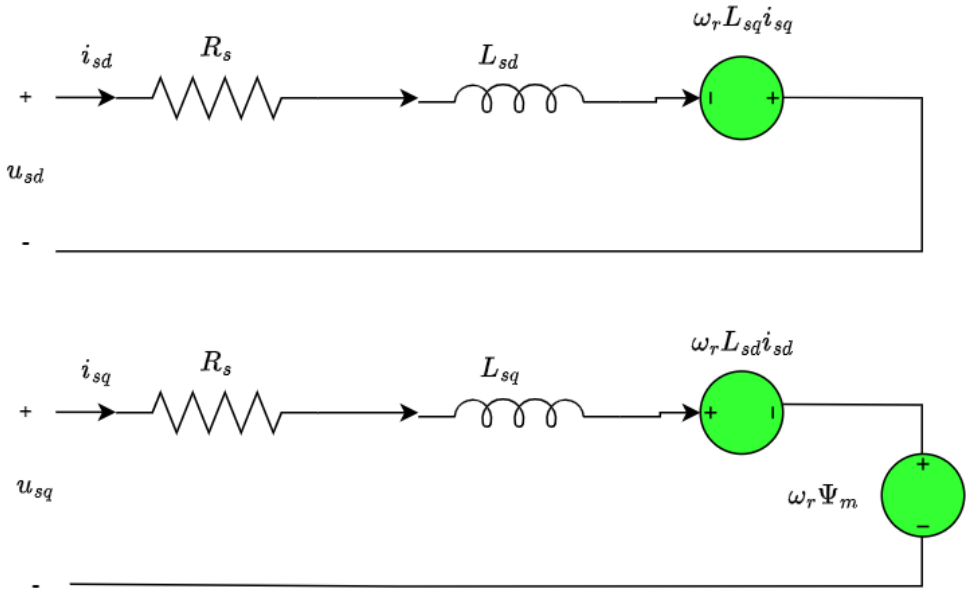

Figure 2.8: Dynamic model in dq-coordinates.

The dynamic model consists of dq-frame stator voltage u_{sd} and u_{sq} [V]; stator dq-currents i_{sd} and i_{sq} [A]; stator dq-inductances L_{sd} and L_{sq} [H]; stator winding resistance R_s [Ω]; magnetic flux linkage ψ_m [Wb] and electrical rotor speed ω_r [rad/s]. From the circuit in Figure 2.8 the stator dq-voltages can be described by the expressions [18]

$$u_{sd} = R_s i_{sd} + L_{sd}\frac{di_{sd}}{dt} - \omega_r L_{sq} i_{sq} \tag{2.22}$$

$$u_{sq} = R_s i_{sq} + L_{sq}\frac{di_{sq}}{dt} - \omega_r L_{sd} i_{sd} + \underbrace{\omega_r \psi_m}_{\text{Back-EMF}} \tag{2.23}$$

where $R_s i_s$ is the resistive voltage drop in the winding. $\omega_r L_s i_s$ is the steady-state voltage drop of the inductances and also the cross-coupling terms between the d- and q-axis. $L_s \frac{di_s}{dt}$ is the transient voltage drop of the inductances. The term $\omega_r \psi_m$ in the q-voltage is the back-EMF which is a motion induced voltage in the motor's winding as described in section 2.4.3.

Furthermore, the mechanical equations of the IPMSM can be expressed as follows [19]

$$T_e = \frac{3n_p}{2}(\underbrace{\Psi_m i_{sq}}_{\substack{\text{Magnet} \\ \text{Torque}}} + \underbrace{(L_{sd} - L_{sq}) i_{sd} i_{sq}}_{\text{Reluctance Torque}}) \tag{2.24}$$

$$\frac{J}{n_p}\frac{dw_r}{dt} = T_e - T_L - \frac{B}{n_p}\omega_r \tag{2.25}$$

$$\frac{d\theta_r}{dt} = w_r \tag{2.26}$$

where:

- T_e is the electromagnetic torque [Nm]
- n_p is the number of pole pairs [-]
- J is the inertia of the IPMSM [kgm^2]
- T_L is the load torque [Nm]
- B is the friction factor [Nm/(rad/s)]

Figure 2.9 visualizes the interplay between the electromagnetic torque produced by the IPMSM, the mechanical rotor speed and the load torque that opposes the produced torque.

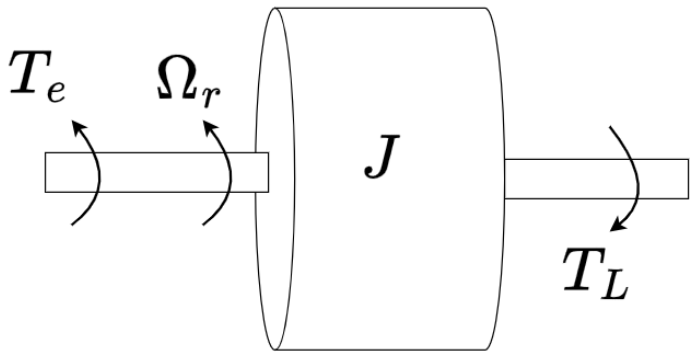

Figure 2.9: Electromagnetic torque T_e and mechanical speed Ω_r [rad/s] produced by the IPMSM versus opposed load torque T_L.

Additionally, the following equations can be used to describe the relationship between electrical and mechanical representations (for one mechanical turn of the rotor multiple electrical turns are being made dependent on the number of pole-pairs n_p)

$$\Phi_r = \frac{\theta_r}{n_p} \tag{2.27}$$

$$\omega_r = \Omega_r n_p \tag{2.28}$$

where Φ_r [rad] is the mechanical rotor position and Ω_r is the mechanical rotor speed. The output power of the IPMSM is calculated by the mechanical properties as

$$P_{out} = T_e \Omega_r = T_e \frac{\omega_r}{n_p} \tag{2.29}$$

where P_{out} [W] is active power.

2.4.6 IPMSM Operating Characteristics and Current Vector Control

The operating range of an IPMSM can be divided into three parts, Maximum Torque Per Ampere (MTPA), Field-Weakening and Maximum Torque Per Volt (MTPV). The need of these current/torque control strategies comes from the fact that the motor operation is constrained by the rated stator current to the motor, and the rated voltage imposed by the constraints of the inverter (maximum DC bus voltage) [20]. Hence, (2.2), (2.4) and (2.5) can be used to calculate the rated voltage dependent on the modulation principle being used for the inverter control. The rated current can be expressed as

$$I_{mag} = \sqrt{I_D^2 + I_Q^2} \leq I_{rated} \tag{2.30}$$

where I_{mag} [A] is the stator current magnitude. The rated voltage can be expressed as

$$U_{mag} = \sqrt{U_D^2 + U_Q^2} \leq U_{rated} \tag{2.31}$$

where U_{mag} [V] is the stator voltage magnitude.

By incorporating (2.31) into the IPMSM stator dq-voltage, (2.22) and (2.23) in steady-state and when neglecting the ohmic voltage drop, the speed-dependent voltage limit ellipses in Figure 2.10 can be drawn where the stator currents are the variables [20].

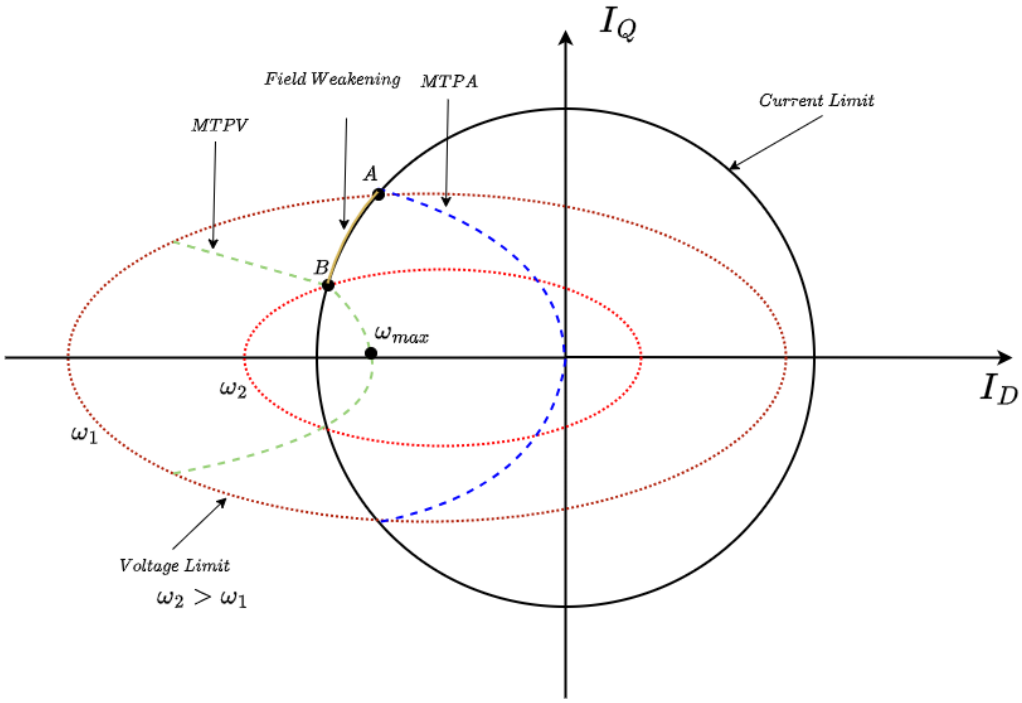

Figure 2.10: IPMSM Operating Characteristics.

The available working region for the IPMSM is within the voltage limit ellipses (for the speeds ω_1 and ω_2 [rad/s]) and the current limit circle. From the origin to point A in Figure 2.10 the MTPA control strategy is employed to select the appropriate i_d and i_q to generate as much torque as possible while minimizing the stator current magnitude. The speed at which the rated torque is achieved (where the rated current and rated voltage intersect in point A in Figure 2.10) is called rated speed.

To exceed the rated speed while still producing maximum torque the field-weakening control strategy must be chosen [20]. This region is from point A to B in Figure 2.10. Subsequently, to obtain speeds up to the maximum point while generating maximum torque the MTPV control strategy needs to be used. This region is depicted between point B and ω_{max} in Figure 2.10.

The above-mentioned regions and current/torque control strategies can be visualized more intuitively by Figure 2.11 below.

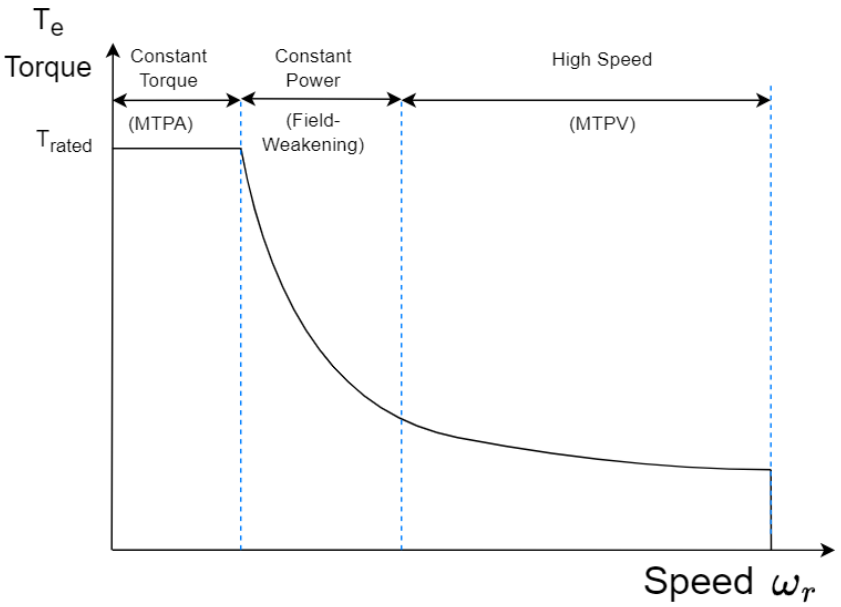

Figure 2.11: IPMSM Speed versus torque graph.

It depicts the motor's operating point and the current/torque control strategy used at that point.

2.4.6.1 MTPA

In the first operating region in Figure 2.11, MTPA, the IPMSM produces the maximum torque while not trespassing the maximum stator current [15]. This strategy minimizes the stator current amplitude while producing a certain torque. This operation is advantageous since the switching losses and conduction losses in the inverter are reduced as well as the resistive losses in the stator winding [21]. The MTPA current trajectory can be employed by calculating the stator current angle such that the stator flux and the magnet flux are at an optimal angle.

The stator currents in the *dq*-frame can be expressed as

$$I_d = I_{mag}cos(\beta) \tag{2.32a}$$

$$I_q = I_{mag}sin(\beta) \tag{2.32b}$$

where β [rad] is the stator current angle. By incorporating (2.32a) and (2.32b) into the torque equation (2.24), it can be rewritten as

$$T_e = \frac{3n_p}{2}(\Psi_m i_{mag}sin(\beta) + (L_{sd} - L_{sq})i_{mag}^2 cos(\beta)sin(\beta)) \tag{2.33}$$

By differentiating (2.33) with respect to β and putting it equal to zero as

$$\frac{\partial T_e}{\partial \beta} = 0 \tag{2.34}$$

the stator current angle β that maximizes the electromagnetic torque T_e can be found. The MTPA expression of the stator current angle becomes

$$\cos(\beta) = -\frac{\Psi_m}{4(L_{sd} - L_{sq})I_{mag}} - \sqrt{\frac{1}{2} + \left(\frac{\Psi_m}{4(L_{sd} - L_{sq})I_{mag}}\right)^2} \tag{2.35}$$

and by utilizing this angle the MTPA control method is employed.

2.4.6.2 Field-Weakening

In the second region in Figure 2.11 where the speed is beyond the rated speed (base speed in the figure) the back-EMF term in (2.23), which is dependent on the rotor speed and the magnetic flux linkage, exceeds the supply voltage which in turn complicates the functioning of the machine [22]. To overcome this issue such that the machine can operate beyond base speed the rotor flux linkage is reduced by decreasing the d-current to a more negative value [22]. To keep the stator current below the rated current the q-current needs to be decreased to a smaller positive value.

2.4.6.3 MTPV

In the third region in Figure 2.11, MTPV, the IPMSM produces the maximum torque while not trespassing the maximum voltage limit [23]. Thereby (2.31) is fulfilled where U_{rated} depends on the battery voltage (U_{DC}) and the modulation principle being used to control the inverter switches [23].

2.5 IPMSM Power Losses

In this section the IPMSM power losses will be covered with the corresponding equations to calculate them.

2.5.1 Copper Losses

Copper losses, or winding losses as they are also referred to, exists both in the stator and in the rotor (if any which depends on the motor at hand). The copper losses can be divided into two parts, DC copper losses and AC copper losses [24]. The DC copper loss is caused by the current flowing through a conductor causing ohmic losses and is independent of the current frequency [24].

The AC losses however, are present due to the harmonic current components [2] and are dependent on the frequency. It can be divided into skin and proximity effects, and circulating current effects as [25]

$$P_c = P_{DC} + P_{skin\ \&\ proximity} + P_{circulating\ current} \tag{2.36}$$

where P_c [W] is the total copper losses. The skin effect is a phenomenon where the current density is larger at the surface of the conducting wire than at the core. With increasing AC frequency the skin depth is reduced, hence the effective area of the wire is reduced and therefore the skin effect is amplified [26]. The proximity effect is when losses in a conducting wire occurs because of an external electromagnetic field generated by surrounding wires [25]. The skin effect and proximity effect impose power losses in terms of Eddy current copper losses [24]. Eddy currents are further explained in section 2.5.2.

Moving on, in operation some of the armature field flux generated by the winding in the stator leaks inside the slots. Hence, some wire bundles experience a different flux linkage which yields a different inductance. This inductance difference between some wire bundles generate circulating currents and these currents are the main contribution to the winding copper losses [25]. The DC winding losses of an electric machine can be calculated as [27]

$$P_{DC} = \frac{3}{2}(i_{sd}^2 + i_{sq}^2)R_s = \frac{3}{2}i_{mag}^2 R_s \tag{2.37}$$

where R_s [Ω] is the resistance.

2.5.2 Iron Losses

Iron losses, or core losses as also referred to, are generated by the alternating magnetic field in the iron core of the electrical machine. The total loss can be divided into three categories by utilizing the classical loss separation model of Bertotti [28]. The three parts in this loss model are Eddy current loss, hysteresis loss and excess loss.

The Eddy current loss originates from Faraday's law of induction which implies that a changing magnetic field will induce an electric field in a conductive material. In turn that electric field induces circulating currents referred to as Eddy currents. The concept is visualized in Figure 2.12.

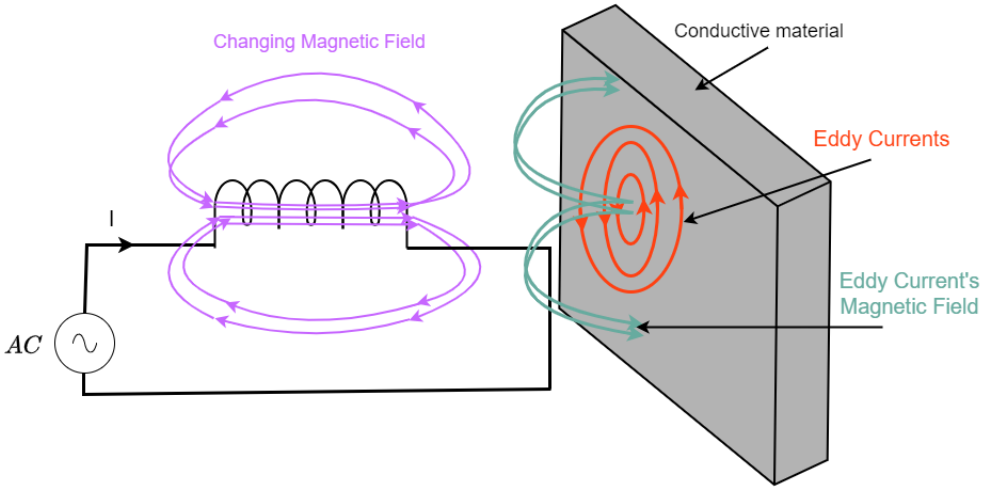

Figure 2.12: Changing magnetic field and induced Eddy currents.

The direction of the Eddy currents in Figure 2.12 is such that their generated magnetic field (Ampere's law) opposes the magnetic field that generated the Eddy currents, according to Lenz's law. These Eddy currents are unwanted currents that consume power which is dissipated as heat. These losses are conventionally limited by introducing laminated cores that restrict the flow of Eddy currents [29].

Hysteresis losses on the other hand, are related to the magnetization and demagnetization of the iron core. When a magnetic material is exposed to a magnetic field the material starts to magnetize. As the magnetic field alternately changes in strength, that material undergoes magnetization and demagnetization cycles. The relationship between the magnetic field strength and the magnetization of the material is described by a hysteresis graph and is depicted in Figure 2.13.

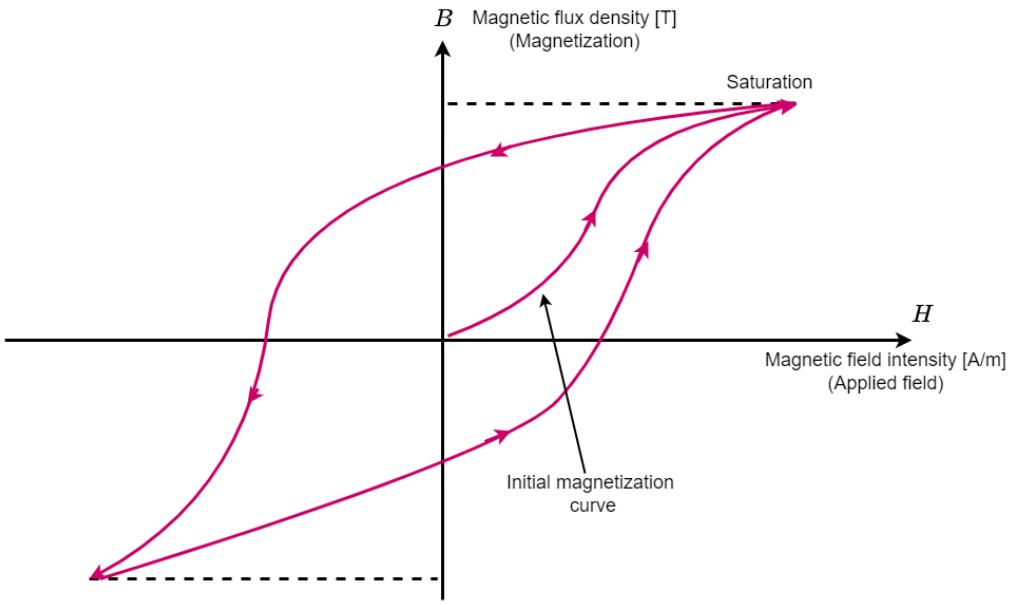

Figure 2.13: Magnetization and demagnetization hysteresis graph.

Essentially, this implies that a stronger opposed magnetic field is needed to demagnetize the material to the original value and hence energy is lost [29]. The hysteresis loss which originates from the discontinuous magnetization process can be obtained by the area of the B-H loop as shown in Figure 2.13 [30].

The total iron loss model and each parts contribution to the total loss, can be expressed by utilizing Steinmetz's equation as [28]

$$P_{Fe} = k_e f^2 B_m^2 + k_h f B_m^{\alpha} + k_a f^{1.5} B_m^{1.5} \tag{2}$$

where k_e, k_h (and α) and k_a are the coefficients for Eddy current loss, hysteresis loss and additional loss respectively. Furthermore, B_m is the amplitude of the magnetic flux density in the motor and f is the corresponding frequency.

2.6 Control System

Getting an IPMSM to steady-state manually can be time consuming, thus a closed-loop control system is needed. As mentioned above, the dq-coordinate frame is most suitable to use when designing the controller and to align the d-axis with the rotor position (FOC) by utilizing the Clarke and Park transformation as described in section 2.4.1. In this frame, it is simpler to calculate the dq-voltages needed to get the desired electromagnetic torque and flux produced in the IPMSM.

The most common control technique used is the Proportional-Integral (PI) controller which is able to get the system to the desired operating point and remove steady-state error while still being fairly simple to tune. The IPMSM:s rotor speed and dq-currents will be controlled by minimizing the error between the actual value and the desired reference.

2.6.1 IPMSM Plant Model

The first step of designing the controller is to state the plant model of the system, in this case the IPMSM. From (2.22) and (2.23) the relation between the applied dq-voltages and the IPMSMs output dq-currents is Laplace transformed to get

$$i_{sd} = \frac{1}{R_s + sL_{sd}}(u_{sd} + \omega_r L_{sq} i_{sq}) \tag{2.38}$$

$$i_{sq} = \frac{1}{R_s + sL_{sd}}(u_{sq} + \omega_r L_{sd} i_{sd} - \omega_r \psi_m) \tag{2.39}$$

which gives the plant models of the IPMSM $G_{cd}(s)$ and $G_{cq}(s)$ as

$$i_{sd} = G_{cd}(s)(u_{sd} + \omega_r L_{sq} i_{sq}) \tag{2.40}$$

$$i_{sq} = G_{cq}(s)(u_{sq} + \omega_r L_{sd} i_{sd} - \omega_r \psi_m) \tag{2.41}$$

also visualized in Figure 2.14.

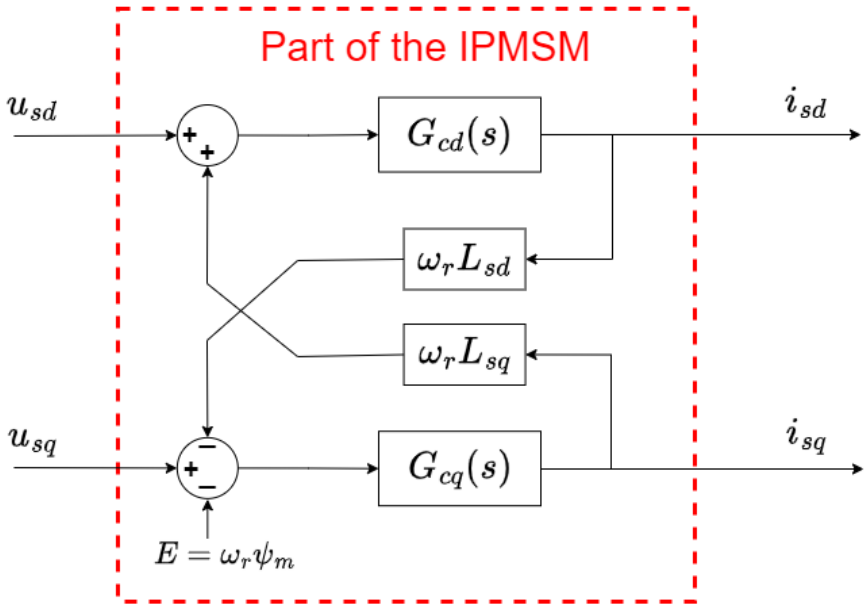

Figure 2.14: IPMSM plant model.

2.6.2 Current Controller

To create a closed-loop control system, the output from the IPMSM i_s is measured and compared to a desired reference current $i_{s,ref}$. The difference between them becomes the error e_c which is fed into the current controller $F_c(s)$ that produces the appropriate voltage u'_s for the IPMSM.

To compensate for the cross-coupling inside of the IPMSM, a corresponding voltage of $\omega_r \hat{L}_s i_s$ [V] is removed from the controllers output, here $\hat{L}_s$ is the estimated inductances. To further increase the robustness against load disturbances, an active damping resistance R_a is added outside of the IPMSM which reduces the output voltage with $i_s R_a$. For the q-current, which is affected by the back-emf, a compensation voltage of $\omega_r \hat{\psi}_m$ is added to the output voltage, $\hat{\psi}_m$ is the estimated magnetic flux. These added compensations creates new plant models from the current controllers perspective, G'_{cd} and G'_{cq}, which are shown in Figure 2.15.

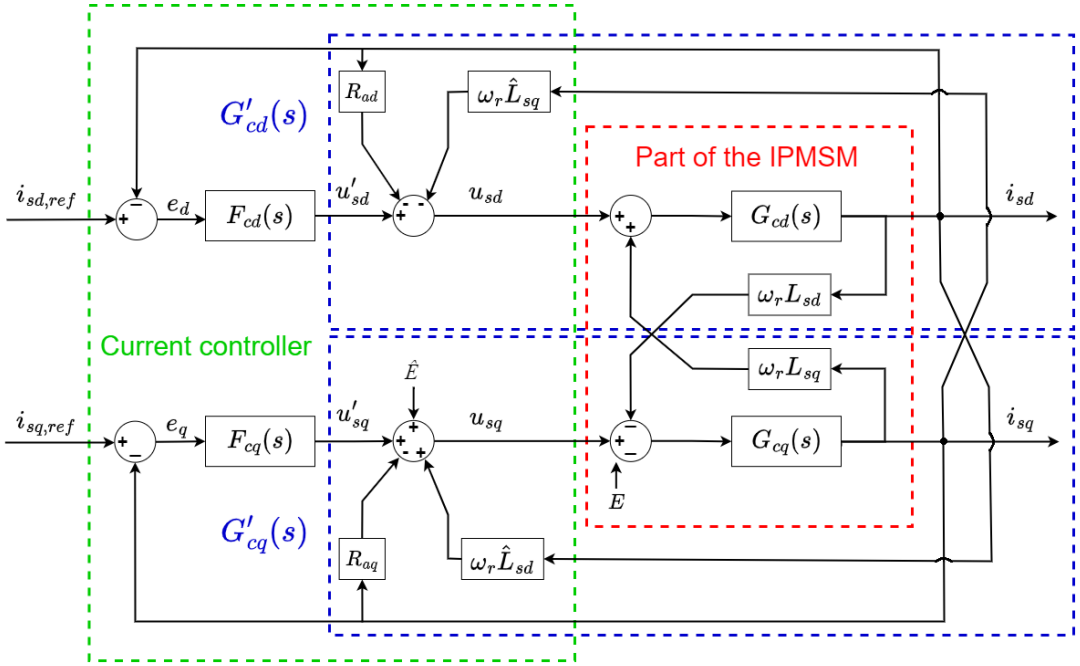

Figure 2.15: Block diagram of extended plant model.

Here $\hat{R}_s$ is estimated stator resistance.

The closed-loop system including the current controller for this model is shown in Figure 2.16.

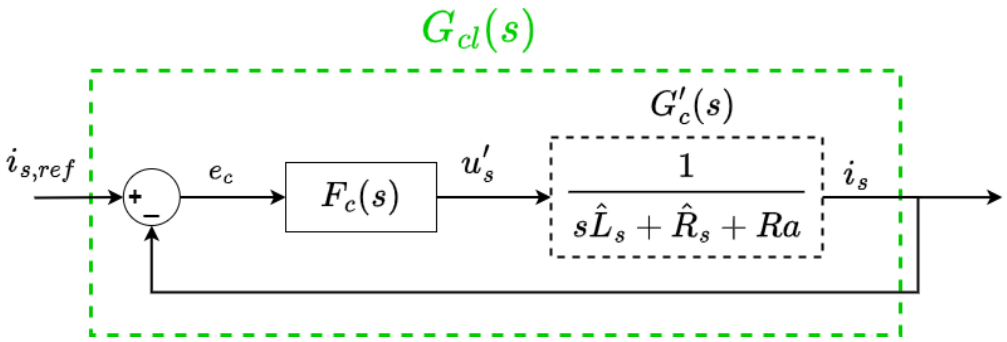

Figure 2.16: Block diagram of closed-loop system.

which also can be expressed according to

$$G_{cl}(s) = \frac{i_s}{i_{s,ref}} = \frac{F_c(s)G'_c(s)}{1 + F_c(s)G'_c(s)} \tag{2.42}$$

2.6.3 PI Controller

A PI controller is a feedback control system that consists of a proportional and an integral part. The proportional output acts directly proportional to the received error, creating immediate error correction. It can however not handle steady-state errors which instead are removed by the integrating part of the controller. This part continuously sums the error to accumulate a controller output that can handle residual error from the set operating point.

The mathematical expression for the controller in the complex domain is

$$F_c(s) = k_{pc} + \frac{k_{ic}}{s} \tag{2.43}$$

where k_{pc} is the proportional gain, k_{ic} is the integral gain and s is the frequency of the signal. The parameters k_{pc} are k_{ic} are calculated by making the closed-loop system $G_{cl}(s)$ a first order low pass filter which can be expressed as

$$F_{LP} = \frac{\alpha_c}{s + \alpha_c} \tag{2.44}$$

where α_c [rad/s] is the chosen bandwidth for the filter. The close-loop system then becomes

$$\begin{aligned} G_{cl}(s) =& \frac{F_c(s)G'_c(s)}{1 + F_c(s)G'_c(s)} = \frac{\alpha_c}{s + \alpha_c} \Rightarrow \\ F_c(s) =& \frac{\alpha_c}{s} G'^{-1}_c(s) = \frac{\alpha_c}{s}(s\hat{L}_s + \hat{R}_s + R_a) = \\ & \alpha_c L_s + \frac{\alpha_c(R_s + R_a)}{s} = k_{pc} + \frac{k_{ic}}{s} \end{aligned} \tag{2.45}$$

It is desired that the extended plant model $G_c'(s)$ should have the same bandwidth as the current controller, which gives

$$G_c'(s) = \frac{1}{s}(s\hat{L}_s + \hat{R}_s + R_a) = \frac{\alpha_c}{s + \alpha_c} \Rightarrow$$
$$\alpha_c = \frac{\hat{R}_s + R_a}{\hat{L}_s} \tag{2.46}$$

Combining (2.45) with (2.46) gives

$$R_a = \alpha_c \hat{L}_s - \hat{R}_s \tag{2.47}$$
$$k_{pc} = \alpha_c \hat{L}_s \tag{2.48}$$
$$k_{ic} = \alpha_c(\hat{R}_s + R_a) \tag{2.49}$$

The controller's output voltage is limited to not exceed the rated voltage from the inverter depending on the modulating principle being used (2.2, 2.4 and 2.5). This limit could make the integrating part of the controller accumulate a large error over time and overload. To compensate for this, a portion of the controllers limited and unlimited output is fed back and removed from the integrating part, also called integrator anti windup.

2.6.4 Speed Controller

It not sufficient to only use a current controller, as the current reference $i_{s,ref}$ needs to be calculated. The solution is to implement a speed PI controller $F_\omega(s)$ which outputs the required torque needed to reach a desired operating speed. MTPA, Field-Weakening or MTPV can then be used to calculate $i_{s,ref}$ from the torque.

Due to the much faster dynamics of the electrical closed-loop system, it can be considered ideal and thus $G_{cl}(s) = 1$. Similar to the current controller, an active damping B_a is added to the speed controllers output which compensates for torque load disturbances. The resulting closed-loop system with the speed controller $G_{cl,\omega}(s)$ is shown in Figure 2.17.

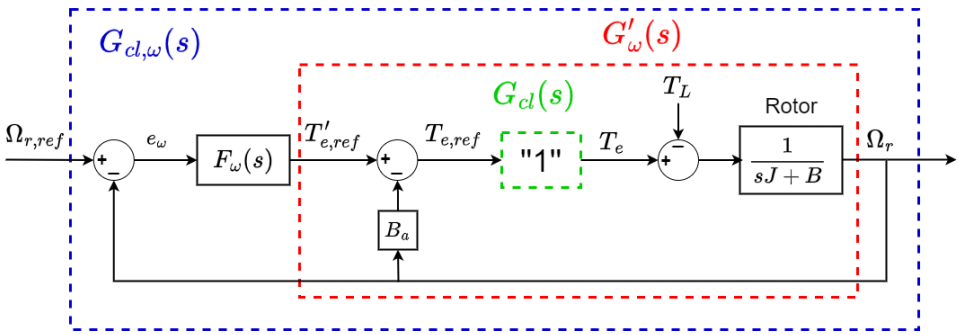

Figure 2.17: Block diagram of closed-loop system $G_{cl,\omega}(s)$.

To find the controller parameters in Figure ($k_{p\omega}$ and $k_{i\omega}$), set the closed-loop system to a first order low pass filter with bandwidth α_ω which gives

$$\begin{aligned} G_{cl,\omega}(s) =& \frac{F_\omega(s)G'_\omega(s)}{1 + F_\omega(s)G'_\omega(s)} = \frac{\alpha_\omega}{s + \alpha_\omega} \Rightarrow \\ F_\omega(s) =& \frac{\alpha_\omega}{s} G'^{-1}_\omega(s) = \frac{\alpha_\omega}{s}(sJ + B + B_a) = \\ =& \alpha_\omega J + \frac{\alpha_\omega(B + B_a)}{s} = k_{p\omega} + \frac{k_{i\omega}}{s} \end{aligned} \tag{2.50}$$

Select the active damping B_a such that $G'_\omega(s)$ has equal bandwidth as the speed controller

$$\alpha_\omega = \frac{B + B_a}{J} \Rightarrow B_a = \alpha_\omega J - B \tag{2.51}$$

Equations (2.50) and (2.51) gives the speed controller gain as

$$k_{p\omega} = J\alpha_\omega \tag{2.52}$$

$$k_{i\omega} = \alpha_\omega(B + B_a) \tag{2.53}$$

3

Case Setup

This chapter will go through the chosen model, parameters and methods used to conduct the study.

3.1 Simulation Model

The simulations and loss calculations for the inverter were conducted in Simulink. The losses in the IPMSM were then calculated afterwards in JMAG. The losses were then investigated separately and combined with respect to switching frequency, modulation principle and Operating Point (OP) to draw conclusions from the simulations.

3.1.1 Simulink

An overview of the system in Simulink is shown in Figure 3.1.

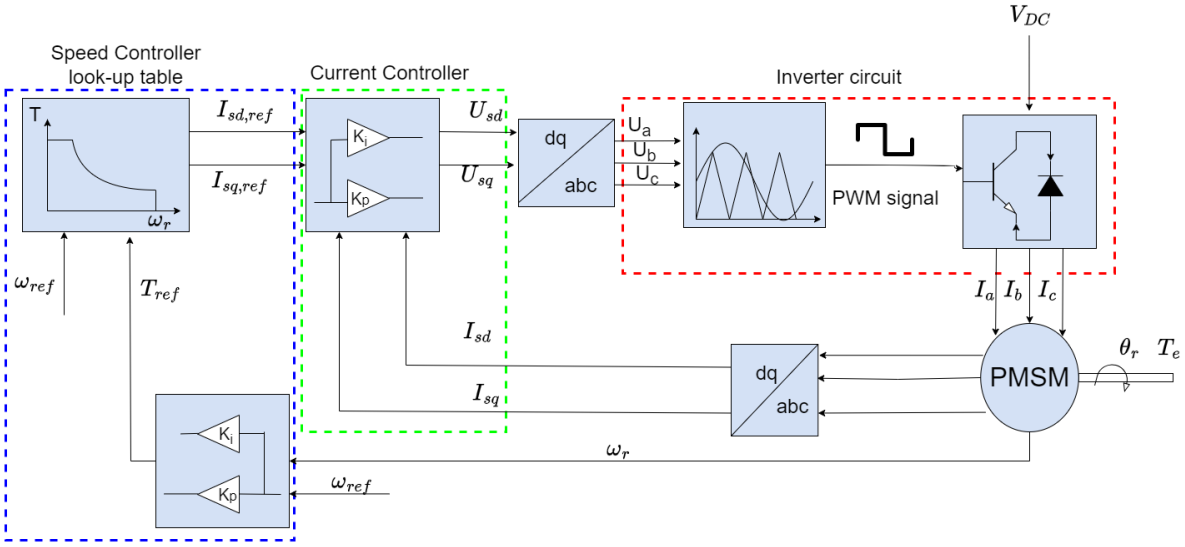

Figure 3.1: Block diagram of Simulink model.

The speed controller was implemented as described in section 2.6.4 with active damping, the mechanical reference speed in Revolutions Per Minute (RPM) along with the actual speed as the inputs.

The output from the speed controller, the required torque, was then fed to the current look-up tables along with the reference speed as the second input. The look-up tables were used to find the desired $i_{sd,ref}$ and $i_{sq,ref}$. The reference currents were then used as inputs to the current controller along with the actual currents.

The current controller was implemented as described in section 2.6.2 with active damping, feed-forward of the cross-coupling term, added back-emf and anti-windup. The current controller also utilized the IPMSM model to calculate the required stator voltages in d- and q-direction. These voltages were transformed to A, B and C quantities by the inverse Park-transform to be used as inputs to the PWM signal generator used to control the transistors in the inverter.

Finally, the three-phase currents from the inverter were sent to the IPMSM model, described by the equations in section 2.4.5. Since the scope of this study did not include any estimation methods, the estimated parameters for the controllers were set equal to the real parameters. Subsequently, new information such as rotor angle, rotor speed, stator currents and electromagnetic torque could be extracted from the IPMSM model described in section 2.4.5 to be used in the control system.

The simulation was conducted for a total of 0.7 seconds with a sample time of 1 µs, with zero initial conditions for both the inverter and IPMSM. The controller adjusted the inverter's voltage output such that the IPMSM got to steady-state for the chosen OP. One fundamental period of the electrical frequency of the three-phase currents in steady-state were then saved and exported as CSV-files to be loaded into JMAG for a new simulation.

3.1.2 JMAG

JMAG is a Finite Element Method (FEM) based software used for electromagnetic calculations for electromechanical components. FEM based calculations discretizes and divides the domain of the problem into smaller elements and finds local solutions to them [31]. The sum of the solutions to all elements, if made small enough, will give a good approximation to the real solution. This method is suitable for solving problems including electromagnetic fields [31].

JMAG has a wide range of usability but for this project it was used to calculate the Eddy current-, hysteresis-, AC- and DC copper losses in the electrical machine. A complete model of the IPMSM with realistic materials and winding was constructed in the program. JMAG was used for the IPMSM losses as it is capable to calculate more precise IPMSM losses than Simulink and Matlab.

3.2 Operating Points

In this work four OP:s for the system were considered, which were regarded as a point at which the electrical machine operates. Hence, the speed that the rotor rotates at and the torque that it produces is the parameters determining the OP. The working points will be referred to as 1, 2, 3 and 4 where OP 1 represents city driving speed where the car is accelerating (low speed and high torque), OP 2 represents highway cruising (high speed and low torque), OP 3 represents country road cruising (moderate speed and low torque), and OP 4 represents highway acceleration (high speed and high torque). The OP:s are numerically represented in Table 3.1.

Table 3.1: OP scenario and numerical representation.

OP	Condition	Speed [RPM]	Torque [Nm]
1	City Driving Acceleration	2500	150
2	Highway Cruise	8000	35
3	Country Road Cruise	5500	30
4	Highway Acceleration	8500	160

These OP:s were chosen since they represent typical operating scenarios of the electrical machine.

3.3 Inverter

Figure 3.2 below illustrates the model of the inverter developed in Simulink.

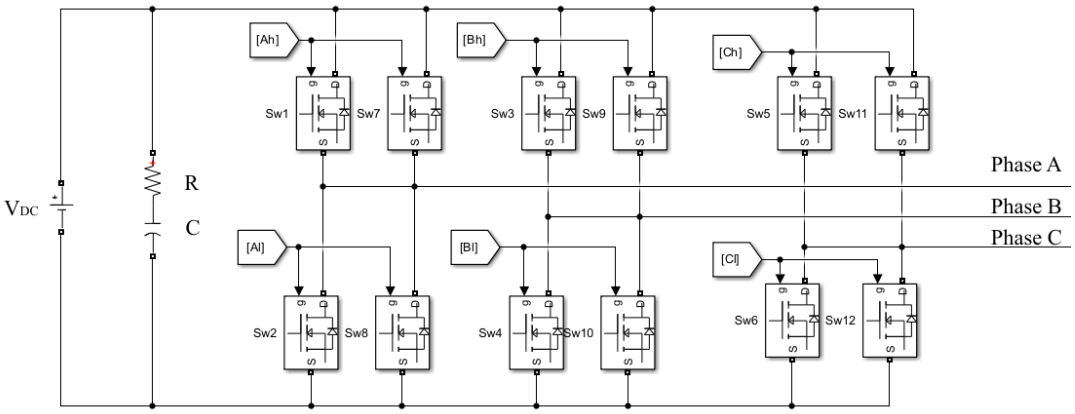

Figure 3.2: Inverter in the Simulink model

Components from the Simscape library were used to capture the electrical properties of the model. The transistors in the model were MOSFET:s of the model Wolfspeed CAB450M12XM3 with built in anti-parallel diodes [32]. The parameters for these components are presented in Table 3.2.

Table 3.2: Wolfspeed CAB450M12XM3 parameters [32].

Parameter	Symbol	Value	Unit	OP
Drain-Source Voltage	$V_{DS,max}$	1200	V	-
Drain Current	$I_{D,max}$	450	A	-
Internal Diode Resistance	$R_{D,on}$	2.5	$m\Omega$	-
MOSFET Resistance	$R_{DS,on}$	2.6	$m\Omega$	-
Turn-On Switching Energy	E_{on}	3.43, 1.89, 1.69, 3.60	mJ	1, 2, 3, 4
Turn-Off Switching Energy	E_{off}	1.00, 0.015, 0.01, 1.15	mJ	1, 2, 3, 4
Internal Diode Reverse Recovery Energy	$E_{D,on}$	0.2	mJ	-

A parallel connection of each power device (MOSFET and anti-parallel diode) was utilized in order to increase the current capability of the inverter. Within these electrical power device blocks, the conduction resistance of the transistors and diodes were added. The parallel connected resistance and capacitor were used to reduce high-frequency noise. Furthermore, the blanking-time was added to the gate signals (A_h, A_l, B_h, B_l, C_h and C_l in Figure 3.2) as discussed in section 2.1. As also mentioned, that introduces a voltage error between the desired voltage suggested by the PWM and the actual voltage out from the inverter. To mitigate this issue (2.1) was used to calculate the signals to be added with the modulation waves.

The signals at the transistor gates were square waves PWM signals, generated according to the SVPWM and DPWM methods described in sections 2.2.2 and 2.2.3. In Figure 3.3, the PWM signal for OP 1 with the SVPWM method is shown.

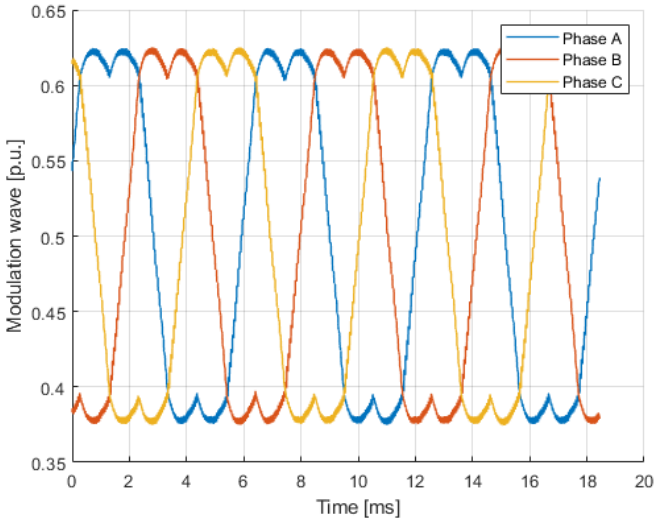

Figure 3.3: Modulation waves for comparison with the carrier wave for the inverter for OP 1, SVPWM at 10 kHz switching frequency.

The carrier wave to be compared with these modulation waves oscillates between 0 and 1 in amplitude. Multiple carrier wave frequencies, i.e. the inverter's switching frequency, were tested for each operating point. More precisely 2.5 kHz, 5 kHz, 7.5

kHz, 10 kHz and 12.5 kHz. In Figure 3.4 the three phase currents coming out from the inverter are visualized.

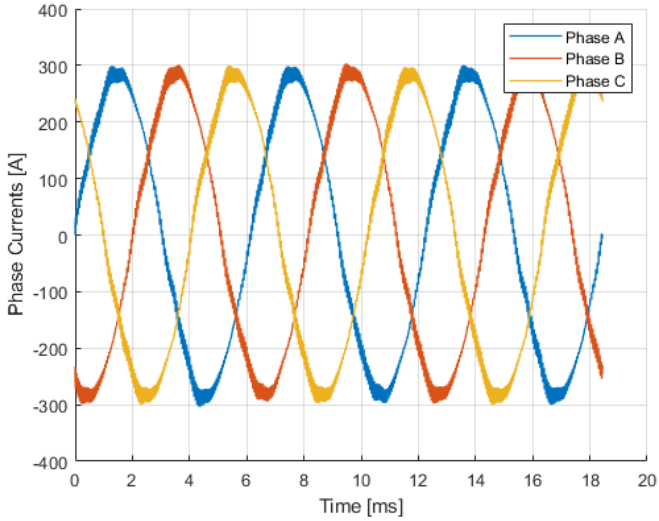

Figure 3.4: Phase currents from the inverter for OP 1, SVPWM at 10 kHz switching frequency.

The currents in Figure 3.4 are the stator currents that induces the rotating magnetic field that the rotor aligns with to produce the electromagnetic torque. In Figure 3.5 the corresponding phase to neutral voltages for phase A and B are depicted.

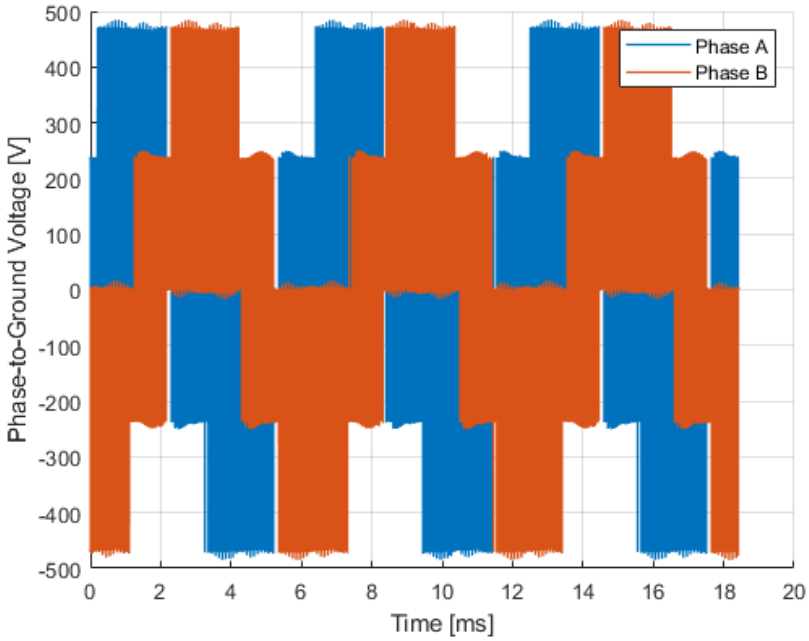

Figure 3.5: Phase-to-Ground voltages from the inverter for OP 1.

Note that the amplitude of the phase voltages in Figure 3.5 are in alignment with Table 2.1 values presented in section 2.1 depending on the switch states.

3.4 Electrical Machine

In the simulation model which was constructed in Simulink the IPMSM block depicted in Figure 3.1 was incorporated through a `JMAG_RT` block which can be seen in Figure 3.6.

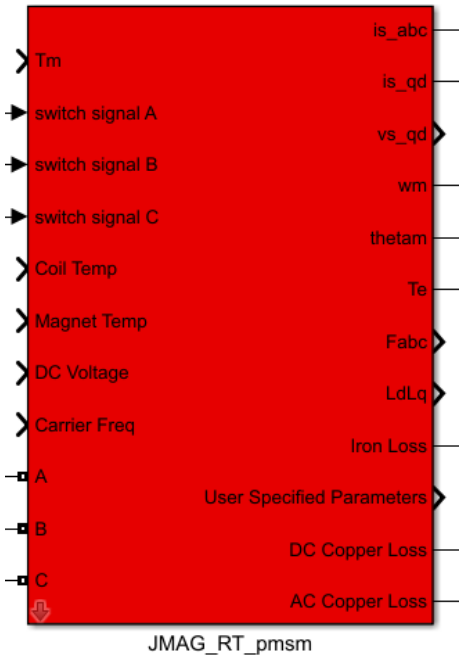

Figure 3.6: IPMSM block in Simulink from the machine model in JMAG.

This block utilizes the torque equation, (2.24), the stator voltage equations in dq-frame (2.22) and (2.23), the mechanical equations (2.25) and (2.26) to describe the electrical and mechanical behavior of the machine. Additionally, it takes into account that the inductances in the dq-frame are dependent on the current and that the inductances and magnetic fluxes are dependent on the stator current angle β.

The electrical machine was first constructed and simulated in JMAG with FEM. The result of this simulation was then converted to a `RTT`-file to be used by the Simulink block. This block then served as a highly accurate process model and look-up table that holds motor characteristics such as varying inductances, magnetic fluxes and torque. The electrical signals coming from the inverter were sent as inputs to this block and it then provided outputs that holds stator currents, stator voltages, rotor speed, rotor angle, electromagnetic torque, magnetic fluxes and inductances.

One fundamental period of the three-phase AC in steady-state that were fed to the IPMSM block in Simulink was also recorded and saved in a CSV-file by Matlab. The current series in this CSV-file was then imported to JMAG for a new simulation used to get more precise loss behaviour of the IPMSM.

3.5 Control System

The control system used was developed according to section 2.6. Due to the large difference in the operating points, different bandwidths α_c and α_ω were used respectively. The references for the controllers were supplied through look-up tables.

3.5.1 Look-up Tables

Instead of calculating the required dq-current references $i_{s,ref}$ at every time step, look up-tables were used to reduce calculation time for the simulation. The two look up-tables consists of the d- and q-currents required for different speeds and torque outputs for the IPMSM. They were generated from earlier simulations conducted on the IPMSM and then normalized with respect to the maximum speed and torque of the IPMSM such that they range between 0 - 1. The resulting look up-tables are shown in Figures 3.7 and 3.8.

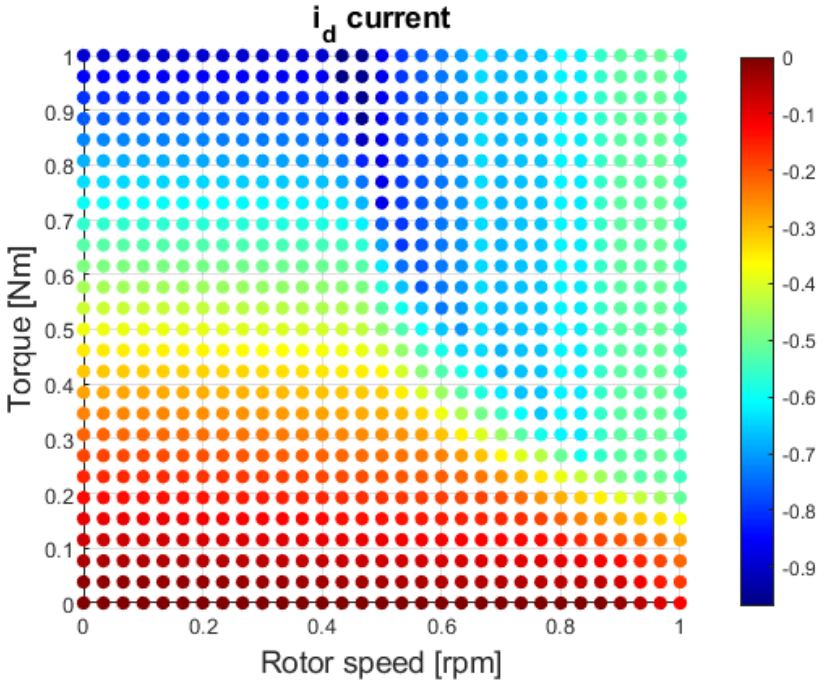

Figure 3.7: Look-up table for $i_{sd,ref}$.

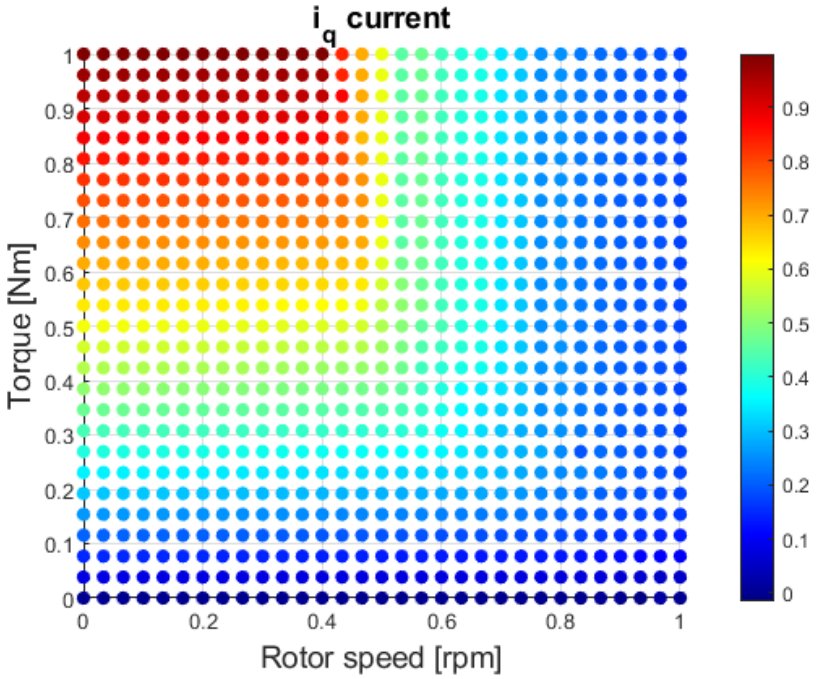

Figure 3.8: Look-up table for $i_{sq,ref}$.

The stator currents are normalized in these plots. The points above the rated torque at each RPM were filled with the rated torque. This is because the look-up table blocks in Simulink needed the input as arrays with values at each point.

3.5.2 Controller Parameters

The current controller and speed controller gains were selected according to the method in section 2.6. The numerical values for the current controller and speed controller are presented in table 3.3 and 3.4 respectively.

Table 3.3: Current Controller parameters

OP	K_{pd}	K_{pq}	K_{id}	K_{iq}	α_c [RPM]
1 - City Driving Acceleration	0.079	0.22	75.3	207.3	954.9
2 - Highway Cruise	0.79	2.17	7526	20732	9549.3
3 - Country Road Cruise	0.79	2.17	7526	20732	9549.3
4 - Highway Acceleration	0.79	2.17	7526	20732	9549.3

Table 3.4: Speed Controller parameters

OP	K_{pw}	K_{iw}	α_w [RPM]
1 - City Driving Acceleration	0.58	4.17	7.16
2 - Highway Cruise	0.26	0.85	3.24
3 - Country Road Cruise	0.24	0.71	2.96
4 - Highway Acceleration	0.3	1.09	3.66

The controller bandwidths for the current and speed controller, α_c and α_w respectively, were found through a trial and error method by analyzing the system behavior for a certain bandwidth. In Figure 3.9 the reference currents versus the actual currents in dq-coordinates are shown.

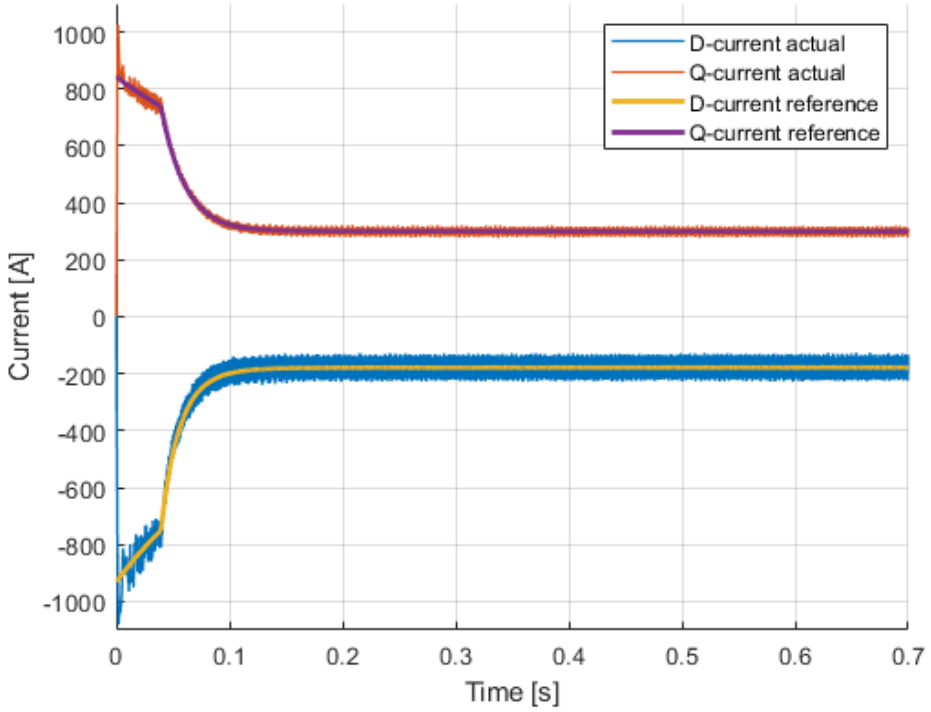

Figure 3.9: Reference vs. actual dq-current for OP 1.

Note that the actual currents stagnates after some time which implies that the IPMSM has reached steady-state and is operating at the desired condition. In Figure 3.10 below the speed characteristics for OP 1 (city driving acceleration) are depicted.

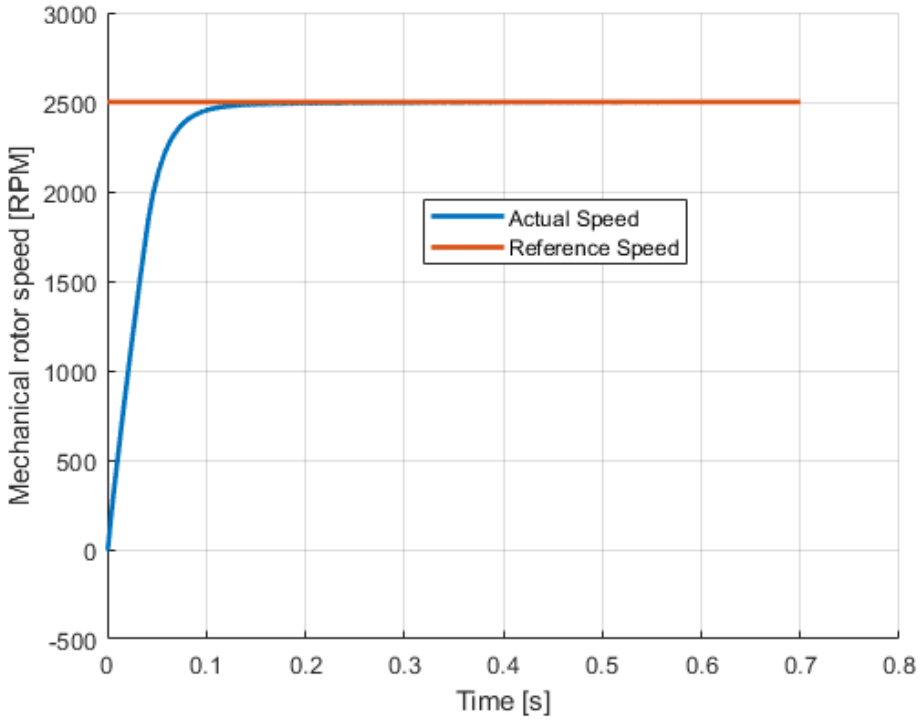

Figure 3.10: Reference vs. actual mechanical rotor speed for OP 1.

The blue line is the actual mechanical rotor speed in RPM whereas the orange one is the reference.

3.6 Inverter Loss Calculation

The inverter losses were calculated according to the method presented in section 2.3 in Matlab. After the simulation, the variables needed for loss calculation were extracted for one fundamental period in steady-state.

For the conduction losses the current flowing through the Drain and Source (D & S) ports in Figure 3.2 were measured and extracted. When the current is positive (flowing from D to S) it flows through the MOSFET only since the anti-parallel diode blocks in the opposite direction. However, when the current flows in the other direction both the MOSFET and anti-parallel diode conducts current if the voltage across the diode exceeds its threshold voltage. The current flowing through the MOSFET and diode were in such scenarios be calculated by

$$\left.\begin{aligned} I_M &= I_{DS} \cdot \frac{R_D}{R_D + R_{DS,on}} \\ I_D &= I_{DS} \cdot \frac{R_{DS,on}}{R_{DS,on} + R_D} \end{aligned}\right\} \text{ for } I_{DS} < 0 \;\&\; V_{DS} < \text{-}U_{D0} \tag{3.1, 3.2}$$

Recalling that U_{D0} is ON state zero-current voltage for the anti-parallel diode, I_D is the diode current, R_D is the diode resistance, $R_{DS,on}$ is the MOSFET resistance. In these equations I_{DS} is the current through the D and S ports in Figure 3.2, note that I_{DS} in section 2.3 was the current through the MOSFET D and S gates. The RMS value of the current through the MOSFET and diode were calculated by squaring all samples, summing them, dividing by the number of samples for one fundamental period and then taking the square root. The average diode current was determined by adding all instantaneous diode current values and dividing by the number of samples. Hence, with the currents calculated, (2.8b) and (2.10b) were applied to get the total conduction losses.

For the switching losses the gate signals controlling the MOSFET:s were extracted for the same fundamental period in steady-state as the other variables, see variable A_h in Figure 3.2. The number of times this signal went from OFF to ON and ON to OFF were counted. Thereafter (2.11) and (2.12) were used where respective energies were retrieved from the data sheet.

3.7 IPMSM Loss Calculation

For the losses in the IPMSM, JMAG was utilized as previously mentioned in section 3.1.2 above. One fundamental period of the three-phase AC in steady-state from Simulink were used as inputs to the electric machine model in JMAG. JMAG divides the resulting losses into three categories; Eddy current losses, hysteresis losses and copper losses. The copper losses are the combined DC- and AC copper losses. JMAG calculates all losses based on FEM, except for the DC copper losses which are calculated according to (2.37).

3.8 Powertrain Energy Efficiency

To determine the energy efficiency η [%] of the entire electric drive system the following equation was used

$$\eta = \frac{P_{out}}{P_{in}} 100\% \tag{3.3}$$

where P_{in} [W] is the electrical power supplied to the EDU and P_{out} [W] is the mechanical power generated by the PMSM. Thereby (2.29) was used for the output power calculation. The input power to the EDU was calculated as

$$P_{in} = U_{in} I_{in} \tag{3.4}$$

where U_{in} and I_{in} are the voltage and current supplied by the battery to the inverter. Since one fundamental period of data was extracted the input power was obtained by taking the mean input power of that period.

The energy efficiency of the power train was also computed through the combined loss model of the inverter and the IPMSM. Hence

$$\eta = \frac{P_{out}}{P_{in}} = \frac{P_{in} - P_{inverter} - P_{IPMSM}}{P_{in}} = \frac{P_{in} - P_{conduction} - P_{sw} - P_{Fe} - P_{copper}}{P_{in}} \tag{3.5}$$

where $P_{inverter}$ [W] is the inverter losses, P_{IPMSM} [W] is the IPMSM losses, $P_{conduction}$ [W] is the inverter conduction losses, P_{sw} [W] is the inverter switching losses, P_{Fe} [W] is the IPMSM iron losses and P_{copper} [W] is the IPMSM copper losses.

3.9 Physical Test Rig

Real physical tests have been conducted on the EDU that the model of this study is built on. The tests were conducted in a lab on an IPMSM, controlled by an inverter which was fed DC from a machine that emulates an EV battery. Sensors were attached to measure the current and voltage fed to the inverter and torque and RPM produced by the IPMSM. Similar to this study, the test rig were set to reach a specified torque and RPM, when steady-state was reached, the power in and out were recorded.

The physical tests were in some ways not as extensive as the tests done in this study. They were only conducted on SVPWM, so there was no available data for DPWM. Additionally, low switching frequencies were not used for higher RPM:s, thus there was no available data for OP 2 and 4 with 2.5 kHz. It were no measurements made between the inverter and IPMSM, therefore the isolated efficiency of the inverter or IPMSM was not available, only the total power consumption for the entire EDU.

4
Results

The results gathered from the simulations are presented in three parts. Firstly, the inverter simulation result from Matlab/Simulink is provided to compare the performance of the different modulation principles (section 4.1). Subsequently, the IPMSM simulation result from JMAG will be presented to view the machine losses in relation to the switching frequencies, modulation principles and OP:s (section 4.2). Thereafter, these results will be combined to supply the total EDU losses and efficiency with respect to switching frequencies, modulation principles and OP:s (section 4.3). Finally, the simulation results from the entire EDU will be compared with the tests conducted on the physical rig to validate the simulation models accuracy (section 4.4). Recalling the OP:s in Table 4.1.

Table 4.1: OP scenario and numerical representation.

OP	Speed [RPM]	Torque [Nm]
1 - City Driving Acceleration	2500	150
2 - Highway Cruise	8000	35
3 - Country Road Cruise	5500	30
4 - Highway Acceleration	8500	160

4.1 Power Losses in the Inverter

The results from the simulations for the different PWM principles are presented in sections 4.1.1 and 4.1.2. An overall comparison between the PWM principles are then investigated in section 4.1.3.

The losses taken into account were the switching and conduction losses of the MOSFET (P_{swM},P_{cM}), and the switching and conduction losses of the anti-parallel diode (P_{swD}, P_{cD}).

4.1.1 SVPWM Simulation Results

In Figure 4.1 the inverter losses for the different OP:s are shown where the SVPWM principle was utilized to control the inverter.

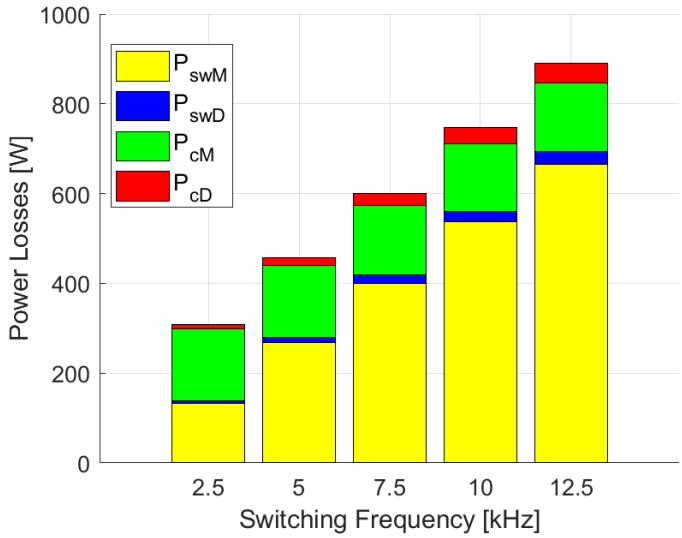

(a) Inverter losses for OP 1 with SVPWM.

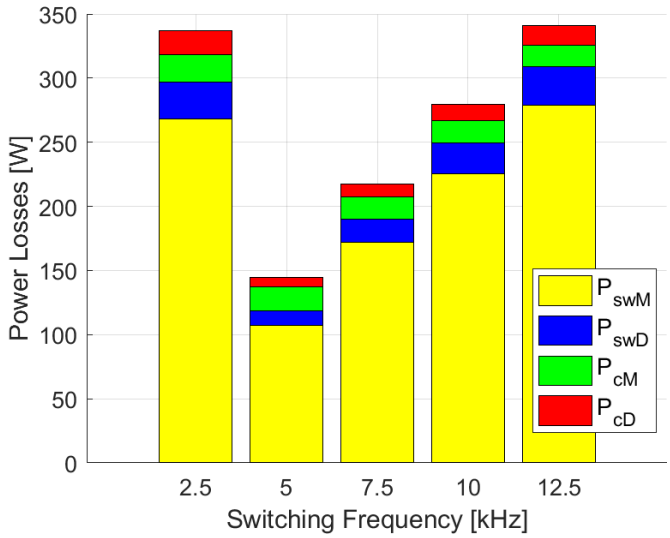

(b) Inverter losses for OP 2 with SVPWM.

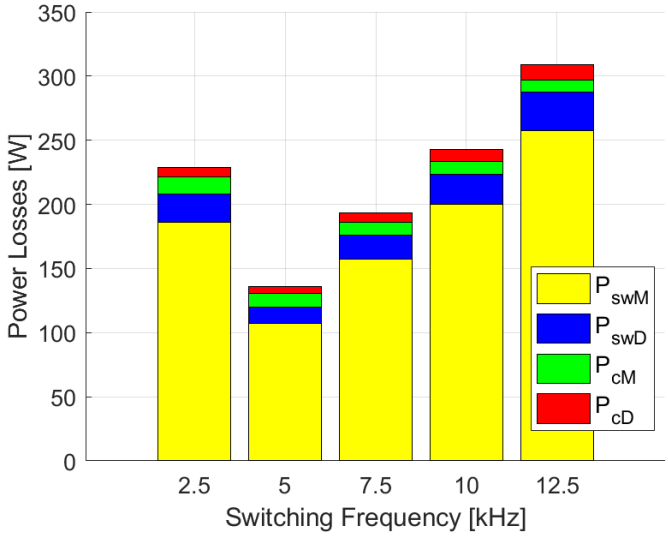

(c) Inverter losses for OP 3 with SVPWM.

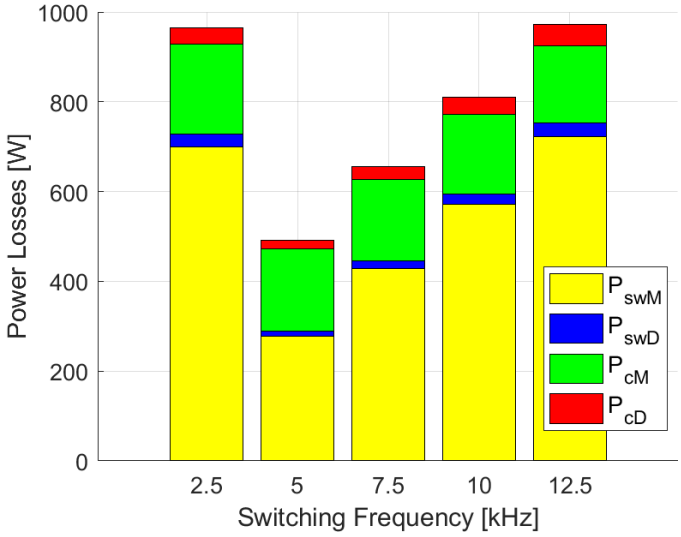

(d) Inverter losses for OP 4 with SVPWM.

Figure 4.1: Inverter losses for different OP:s with SVPWM.

The total power losses for all OP:s increases proportionally to the switching frequency as expected, with an outlying switching frequency of 2.5 kHz for the OP:s 2, 3 and 4. It can also be seen that the conduction losses for the diodes increase linearly with increasing switching frequency. The OP:s with higher torque (1 & 4) requires a larger current which is seen in their increased conduction losses.

4.1.2 DPWM Simulation Results

In Figure 4.2 the inverter losses for the different OP:s are shown where the DPWM principle was utilized.

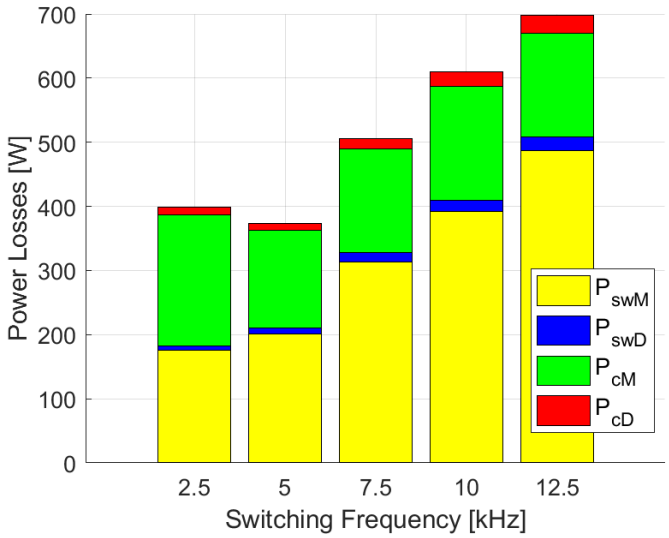

(a) Inverter losses for OP 1 with DPWM.

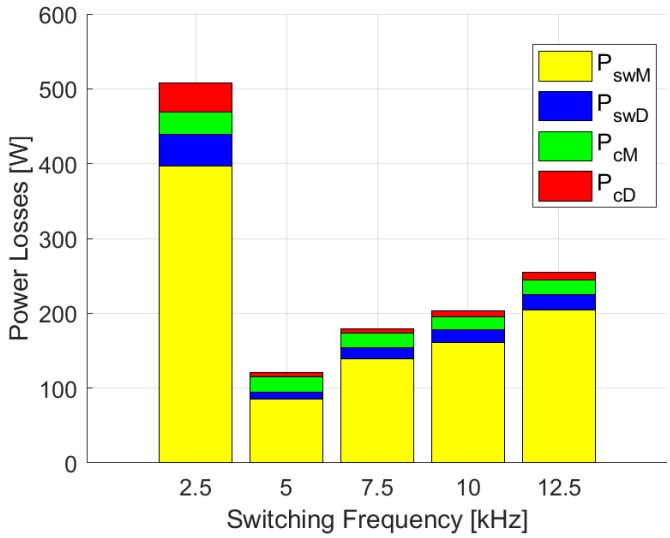

(b) Inverter losses for OP 2 with DPWM.

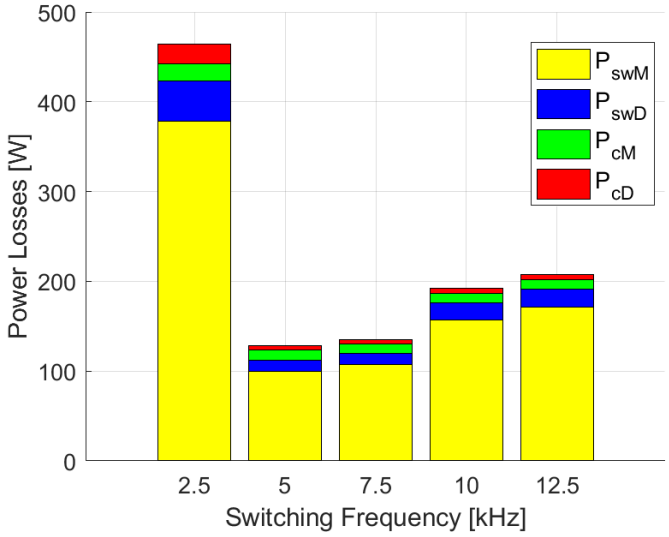

(c) Inverter losses for OP 3 with DPWM.

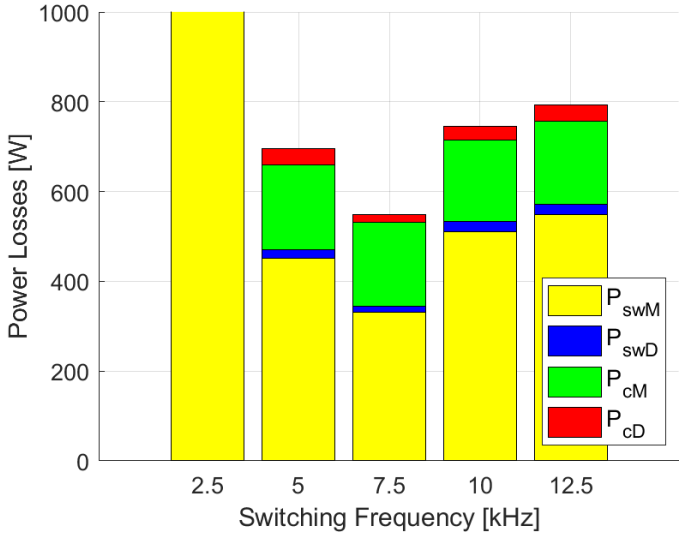

(d) Inverter losses for OP 4 with DPWM.

Figure 4.2: Inverter losses for different OP:s with DPWM.

This modulation principle has an overall similar loss behaviour as for SVPWM. The 2.5 kHz outliers for OP:s 2, 3 and 4 have much larger power losses. The switching losses increases with the switching frequency, same as for the SVPWM results, since it generates more ON and OFF switches of the MOSFET:s and diodes in the inverter, which in turn is associated with energy consumption.

4.1.3 Inverter Loss Comparison

Figure 4.3 shows a total inverter loss comparison of the two PWM principles from the simulations.

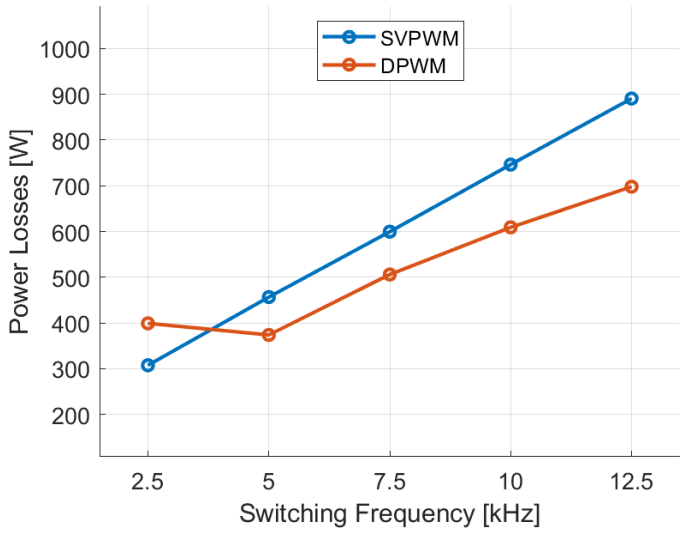

(a) Total inverter losses for OP 1.

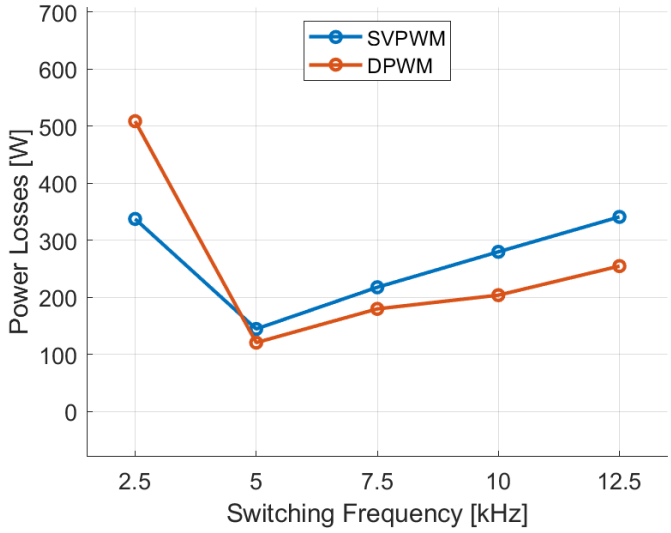

(b) Total inverter losses for OP 2.

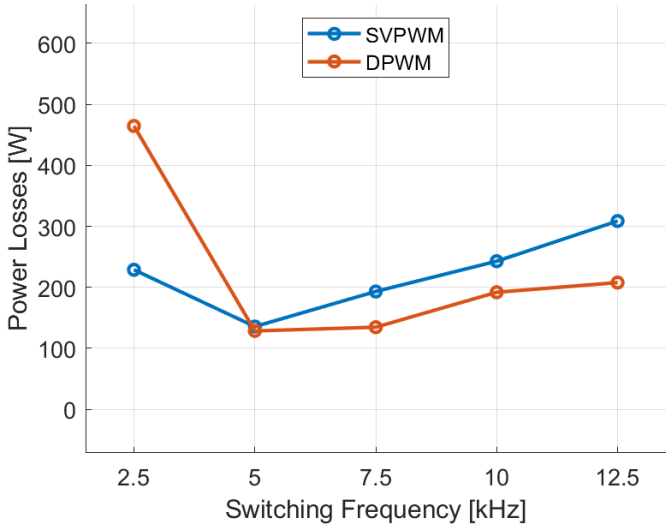

(c) Total inverter losses for OP 3.

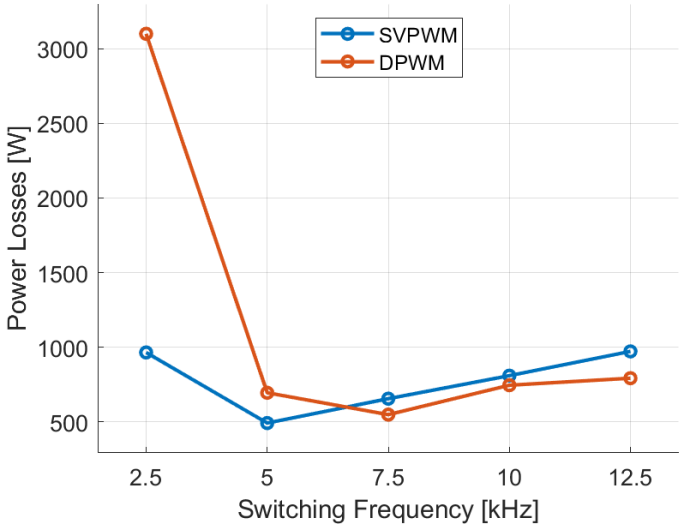

(d) Total inverter losses for OP 4.

Figure 4.3: Total inverter losses for different OP:s and investigated PWM principles.

At 5 kHz and above, DPWM has lower losses for all OP:s, except OP 4 where this happens at 7.5 kHz. SVPWM has a more linear behaviour compared to DPWM, excluding 2.5 kHz for OP:s 2, 3 and 4.

4.2 Power Losses in the IPMSM

The losses taken into account in the electrical machine were Eddy current losses, hysteresis losses and the combined DC- and AC copper losses.

4.2.1 SVPWM Simulation Results

The losses with SVPWM for the IPMSM are shown in Figure 4.4.

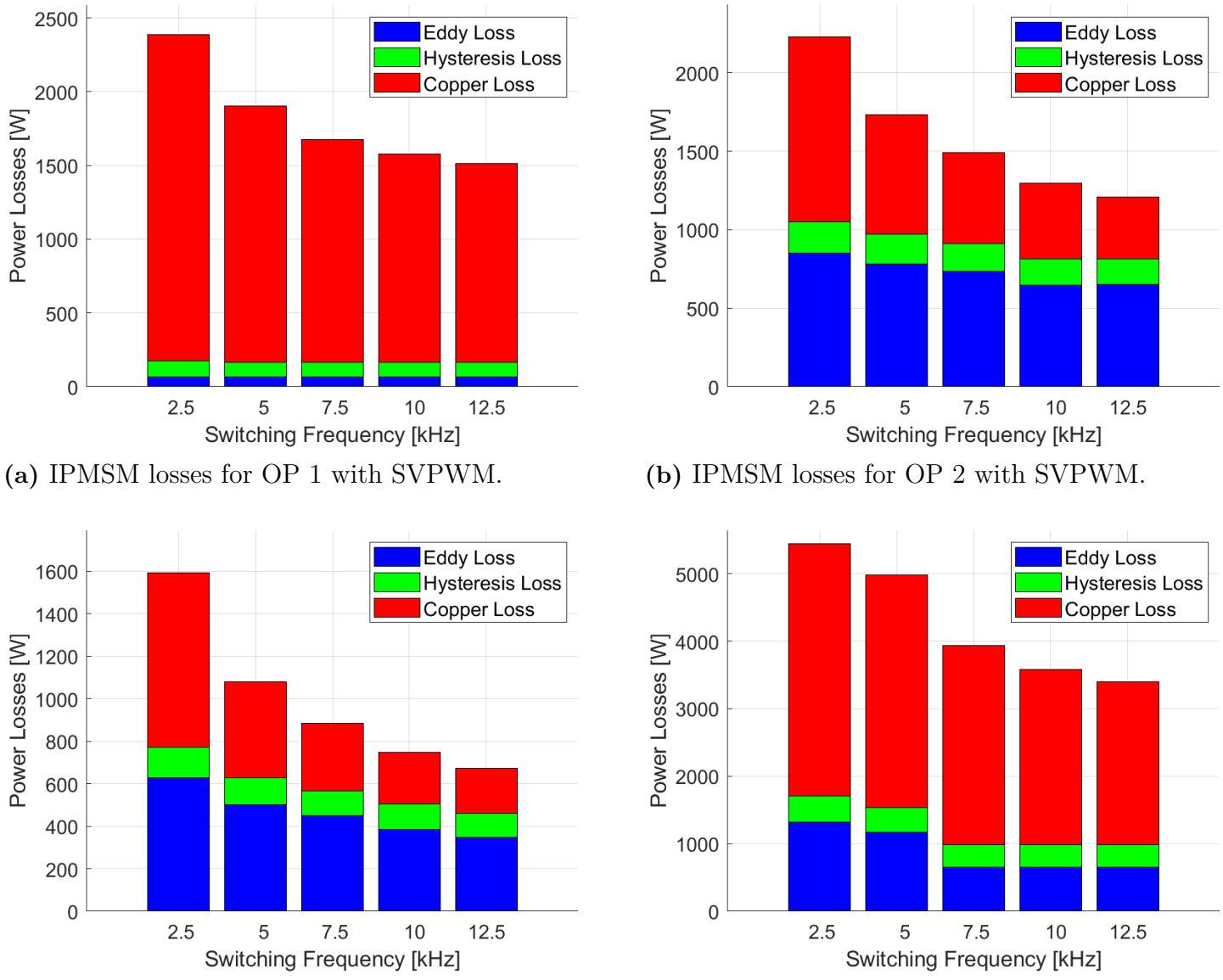

(a) IPMSM losses for OP 1 with SVPWM.

(b) IPMSM losses for OP 2 with SVPWM.

(c) IPMSM losses for OP 3 with SVPWM.

(d) IPMSM losses for OP 4 with SVPWM.

Figure 4.4: IPMSM losses for different OP:s with SVPWM.

The large copper losses in OP 1 and 4 is due to the higher currents for these OP:s. The Eddy current- and hysteresis losses for OP 2 and 4, with high RPM, are larger since these are dependent on the electrical frequency of the rotor.

4.2.2 DPWM Simulation Results

The different losses in the IPMSM for DPWM principle is shown in Figure 4.5.

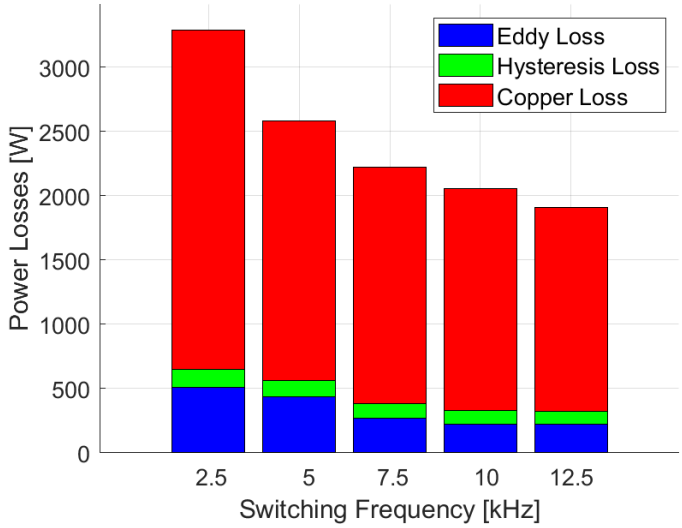

(a) IPMSM losses for OP 1 with DPWM.

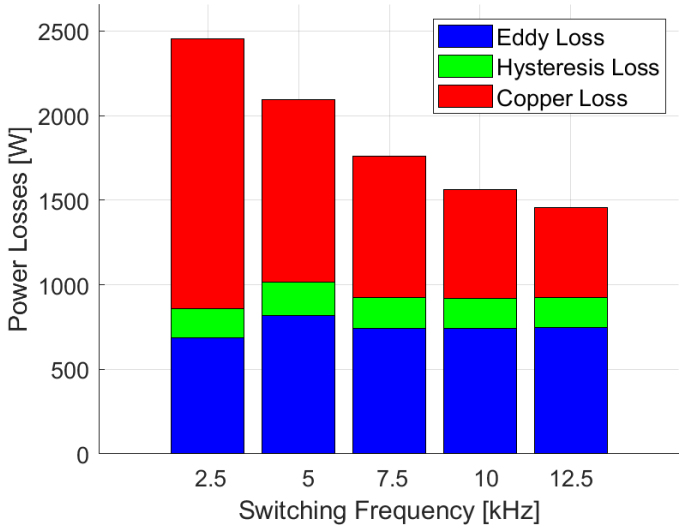

(b) IPMSM losses for OP 2 with DPWM.

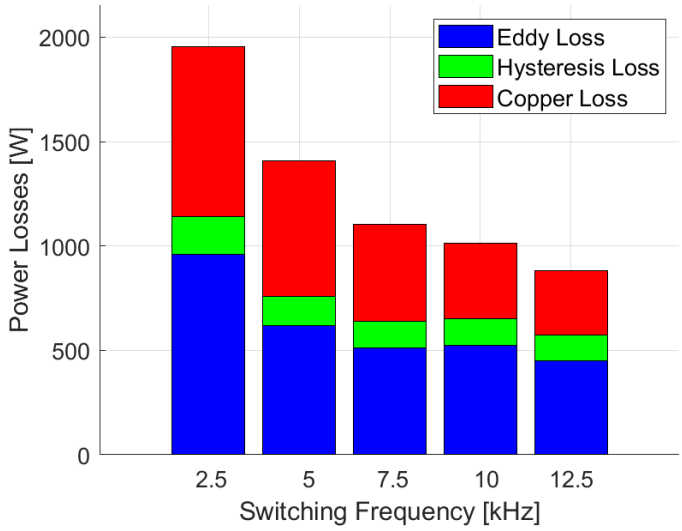

(c) IPMSM losses for OP 3 with DPWM.

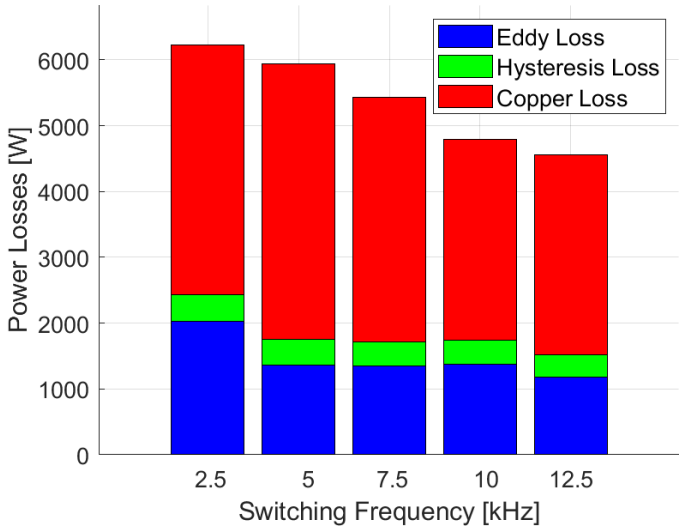

(d) IPMSM losses for OP 4 with DPWM.

Figure 4.5: IPMSM losses for different OP:s with DPWM.

The graphs shows a pattern similar to SVPWM except that the overall machine losses are larger for DPWM because of more phase-current ripple.

4.2.3 IPMSM Loss Comparison

Figure 4.6 shows a comparison between the two PWM principles total IPMSM losses.

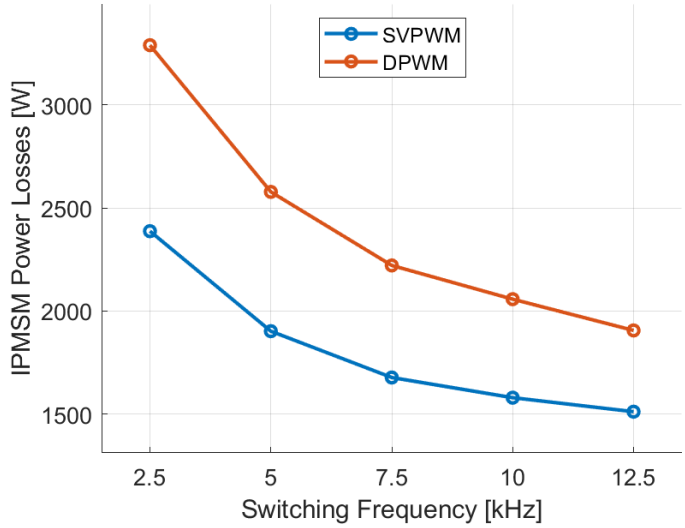

(a) IPMSM loss comparison for OP 1.

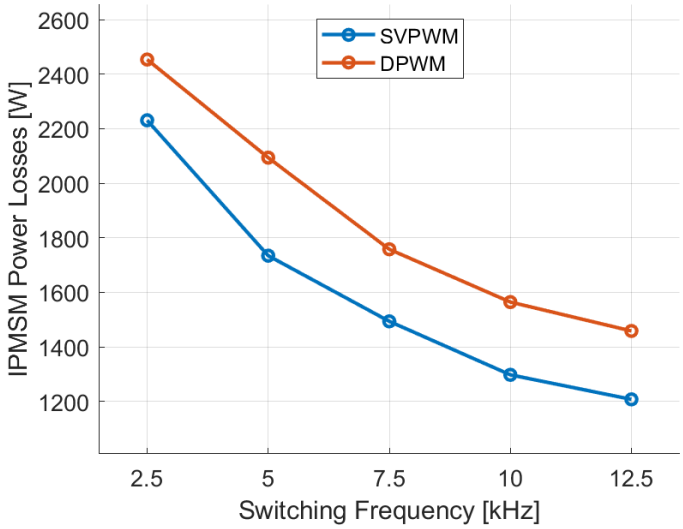

(b) IPMSM loss comparison for OP 2.

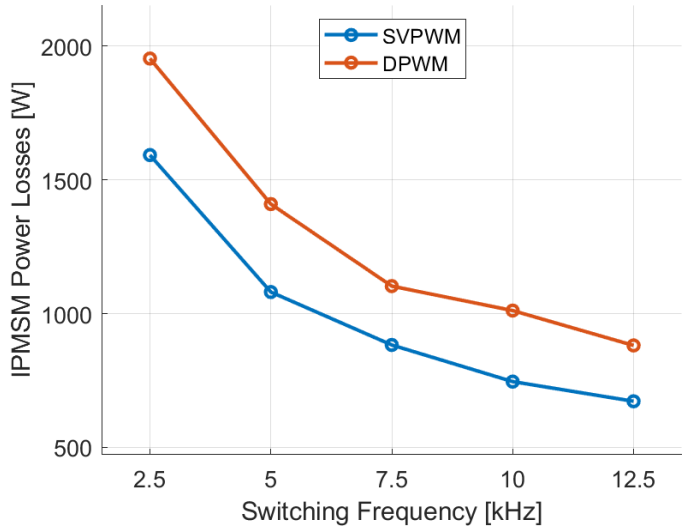

(c) IPMSM loss comparison for OP 3.

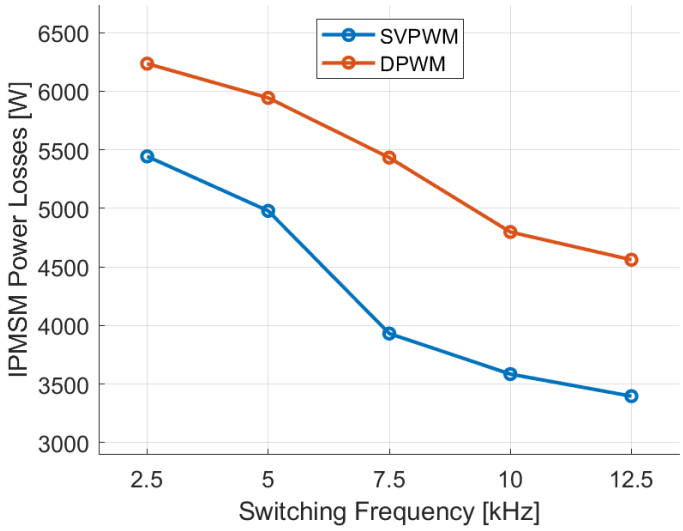

(d) IPMSM loss for comparison OP 4.

Figure 4.6: Total IPMSM loss comparison for different OP:s.

It is clear that SVPWM has smaller losses in the electrical machine for all OP:s and switching frequencies.

4.3 Total Power Loss Comparison

The total losses for the entire EDU is presented and compared in this section.

4.3.1 SVPWM

Figure 4.7 shows the inverter, IPMSM and combined power losses for all for OP:s with SVPWM.

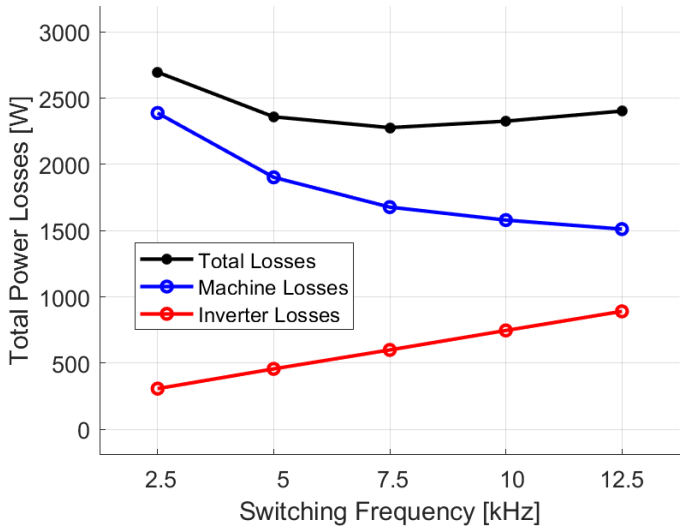

(a) Total losses for OP 1 with SVPWM.

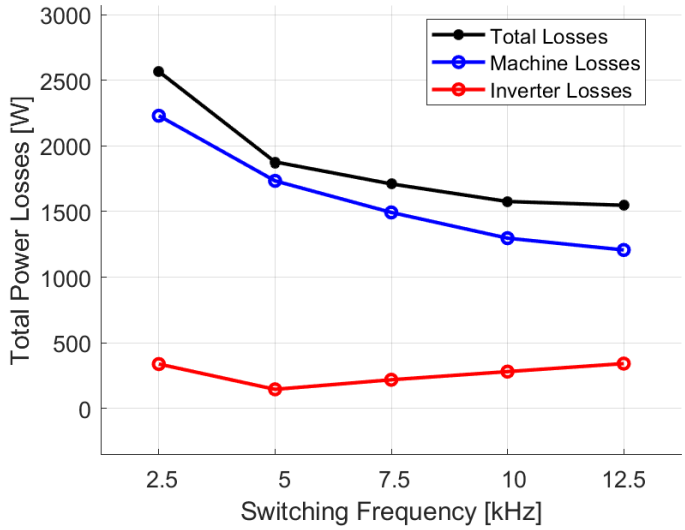

(b) Total losses for OP 2 with SVPWM.

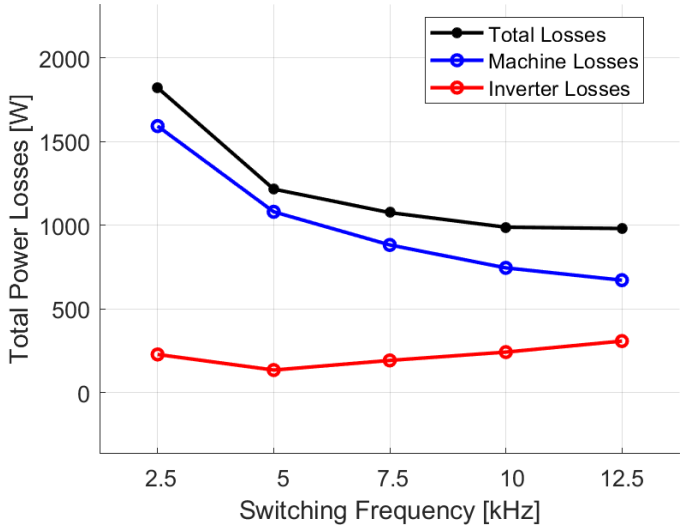

(c) Total losses for OP 3 with SVPWM.

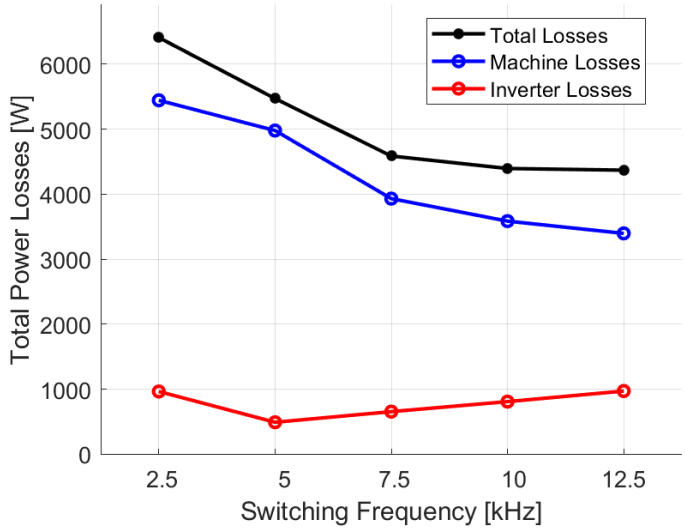

(d) Total losses for OP 4 with SVPWM.

Figure 4.7: Total losses for different OP:swith SVPWM.

As expected the inverter losses increase linearly with the switching frequency whereas the machine losses decrease with increased switching frequency.

4.3.2 DPWM

The total EDU losses for the different OP:s with DPWM is shown in Figure 4.8.

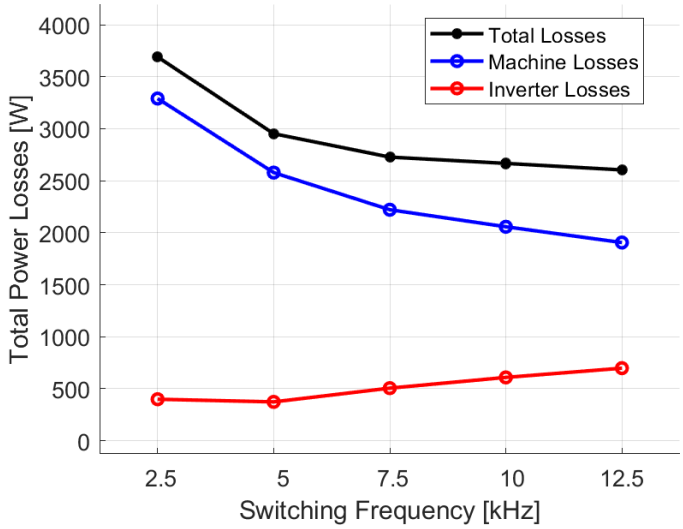

(a) Total losses for OP 1 with DPWM.

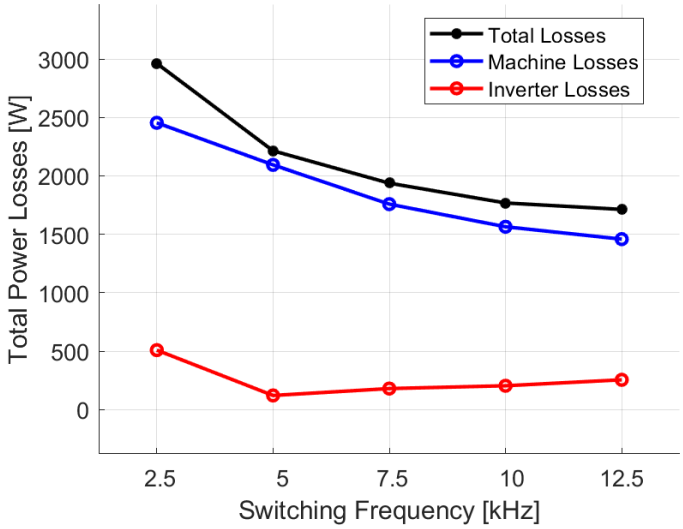

(b) Total losses for OP 2 with DPWM.

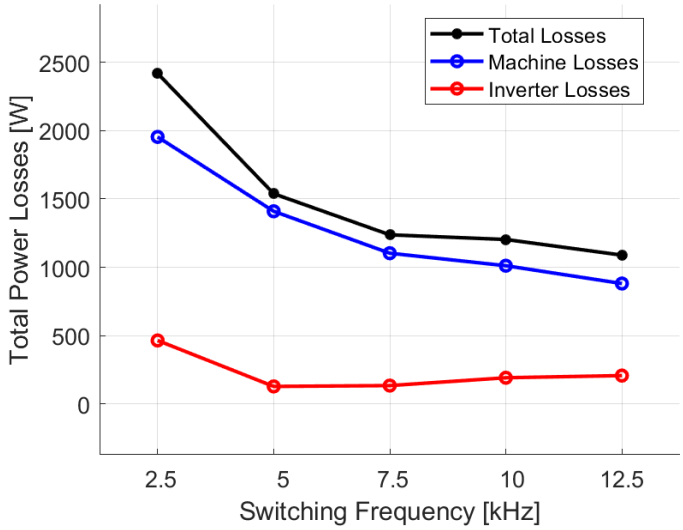

(c) Total losses for OP 3 with DPWM.

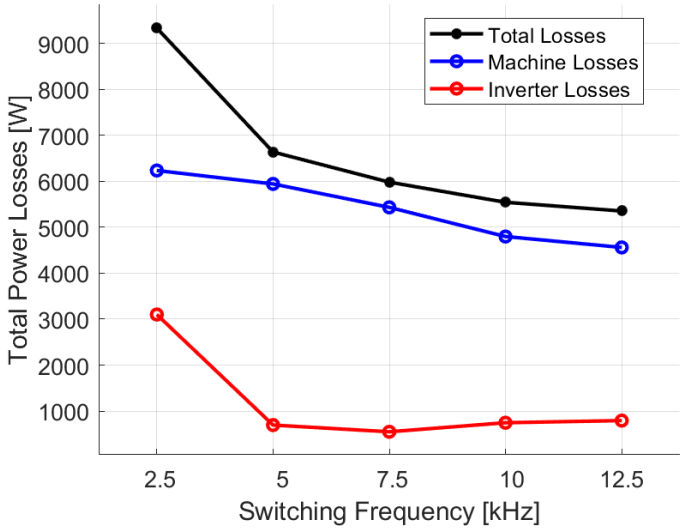

(d) IPMSM losses for OP 4 with DPWM.

Figure 4.8: Total losses for different OP:s with DPWM.

The same behavior as for the EDU losses with SVPWM can be seen in Figure 4.8 but with overall larger machine losses and smaller inverter losses.

4.3.3 SVPWM vs DPWM

Comparisons of the total EDU loss for the two PWM principles are shown in Figure 4.9.

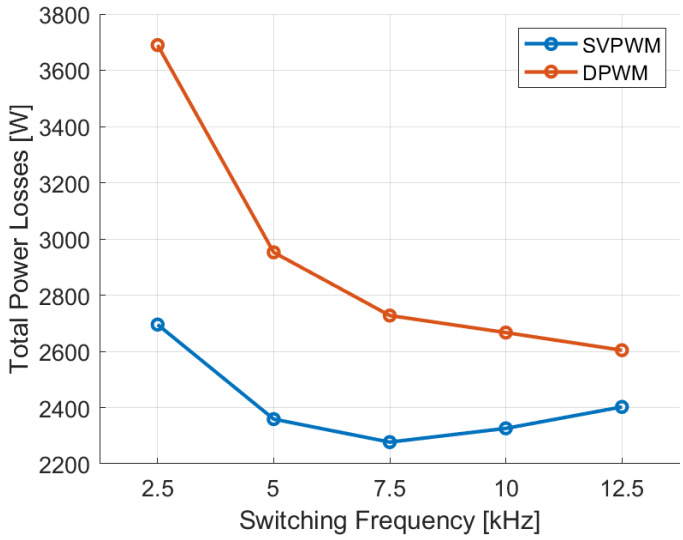

(a) Total loss comparison for OP 1.

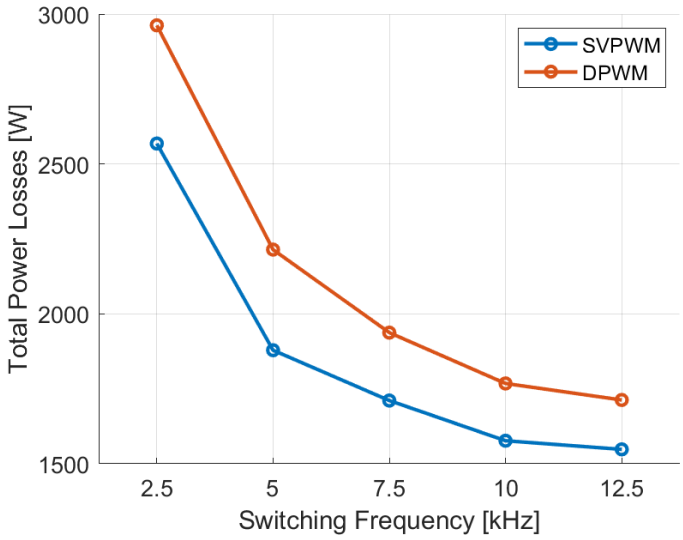

(b) Total loss comparison for OP 2.

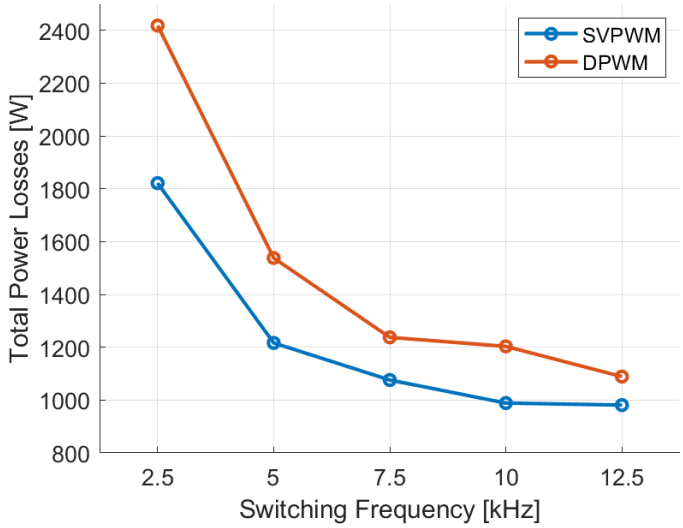

(c) Total loss comparison for OP 3.

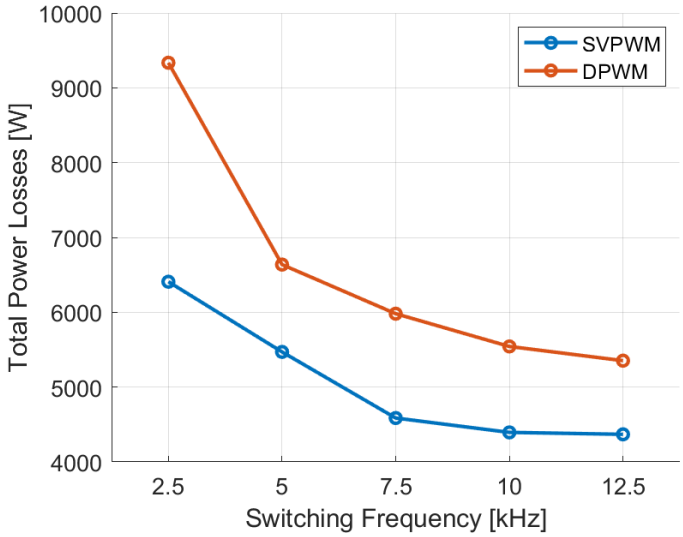

(d) IPMSM loss for comparison OP 4.

Figure 4.9: Total loss comparison for different OP:s.

SVPWM is more power efficient for almost all OP:s and switching frequencies, the difference gets smaller for higher switching frequencies.

4.4 Efficiency Comparison

A comparison with physical tests is shown in Figure 4.10. The residual is displayed as the difference in percentage points between the total EDU power efficiency of the physical tests and simulations. As mentioned in section 3.9, no data is available for OP 2 and 4 with a switching frequency of 2.5 kHz so these points have been excluded from the graph.

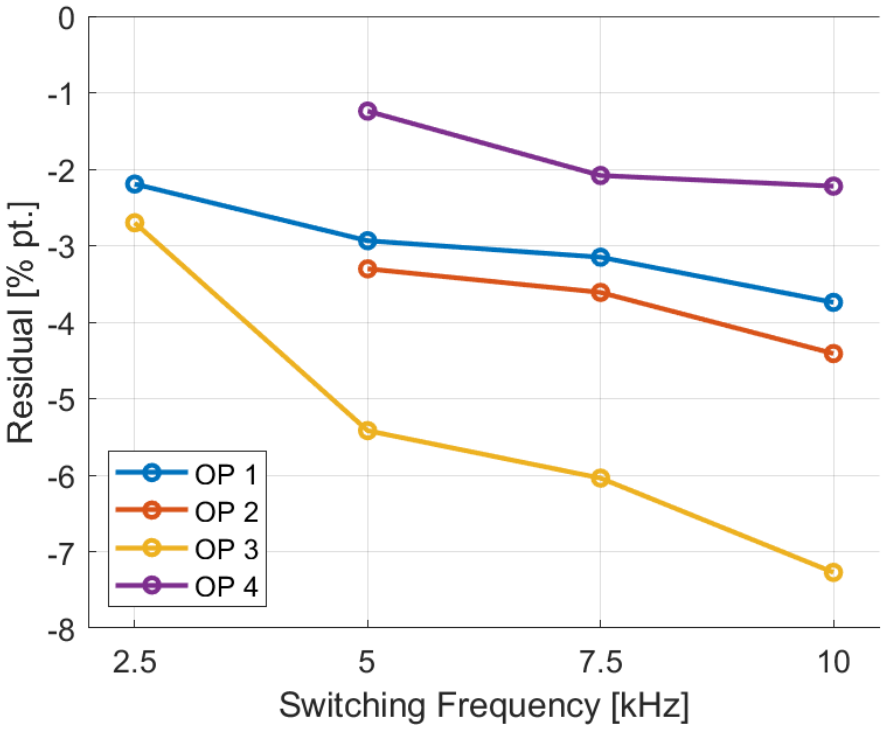

Figure 4.10: Total efficiency comparison for all OP:s with 10 kHz SVPWM.

One trend that can be seen is that the residual increases with the switching frequency. Another trend is that the overall residual is lower for OP:s with lower torque. Arranging the OP:s from highest to lowest torque gives the order 4, 1, 2, and 3, the same order which can be seen in the graph.

5
Analysis

The results from the study are further analysed in this chapter. Some recommendations on future studies that can be conducted based on this thesis are also presented.

5.1 Switching Frequency

Both modulation principles show similar behavior in how their losses depend on the switching frequency. For the inverter it is a linear behaviour with the total power loss increasing with the switching frequency when disregarding the 2.5 kHz outliers. The outlying losses at 2.5 kHz are likely due to that the PWM signals fundamental frequency, which correlates to the electrical frequency, is too large for the switching frequency to match. This mismatch generates a lot of redundant ON and OFF switches which brings the large amount of switching losses. This reason also explains why this behavior is not present for OP 1 since the electrical frequency is small enough for this OP compared to the 2.5 kHz switching frequency.

As mentioned in the results the diode conduction losses increase linearly with the switching frequency. This originates from the fact that when the switching frequency increases, more ON and OFF switches occurs. Between each transition a blanking time is present during which the diodes conduct current, hence, the increase in diode conduction losses is correspondent to the decrease in MOSFET conduction losses.

The losses in the electrical machine decrease with increasing switching frequency. This is expected as a higher switching frequency generates smoother three-phase currents for the IPMSM that has less high frequency noise which gives smaller Eddy current- and AC losses. The total losses in Figure 4.9 shows that the optimal switching frequency is 7.5 kHz for OP 1, with lowest RPM. A switching frequency of 10 to 12.5 kHz were more power efficient to use for the other OP:s.

The results show that having a switching frequency that varies depending on driving conditions is beneficial for power efficiency. However, more OP:s and switching frequencies needs to be examined before a control system for dynamic switching frequency can be developed. The main limitation on how many OP:s that were studied in this thesis were the long simulation times for the IPMSM losses in JMAG. Five different switching frequencies for one OP took around 30 hours to simulate, so a future project would be to simulate more OP:s and switching frequencies.

5.2 Modulation Principle

The results clearly show that DPWM is overall more power efficient for the inverter, with lower losses at switching frequencies above 2.5 kHz. However, it results in greater power losses in the electrical machine, creating a trade-off between inverter and machine losses. The total loss comparison in Figure 4.9 show that DPWM generally has smaller total losses for higher switching frequencies. Although, the lowest total loss is found with SVPWM for all switching frequencies and OP:s.

During the development of the EDU it was noticed that DPWM was harder to control, since the controller values required more fine-tuning. This is not unexpected as the discontinuous "jumps" in the DPWM signal yielded spikes in the three-phase currents that the controller acted on. Further development of the controller could lead to less noisy currents for the IPMSM which in turn gives lower IPMSM losses, making it desirable to investigate in further studies.

As stated in section 2.2.3 it should also be noted that different types of DPWM principles exists, which differs in how much the modulation wave is phase-shifted with respect to the original phase reference. Studies show that they are more or less power efficient at different operating conditions. Therefore a further development of this thesis could be to compare the efficiency of the different DPWM principles with each other.

5.3 Comparison with Physical Model

The overall agreement between our simulation model and the real physical tests are quite good, with an average difference of 3.5 % points. The first trend observed in the results is that the simulation model has lower total losses with increasing switching frequencies, since the difference to the physical results increases. This is an indication that the model has an error that depends on the switching losses in the inverter and/or Eddy current- and AC copper losses in the IPMSM.

The other trend show that the curves are shifted down depending on the torque required for an OP, a lower torque gives an overall lower shifted curve in the graph. This indicates that the losses in our models that are dependent on current, i.e. conduction losses in the inverter and copper losses in the IPMSM, are lower than the same losses in the physical tests.

Since it does not exist any loss data for the inverter and IPMSM individually, we cannot further identify in which parts of the model these errors happens. Further development of the simulation model would require more test data from the physical rig. To enhance the performance of the model, further studies could also incorporate the thermal behavior of the inverter to more accurately capture the inverter losses.

6
Conclusion

The results show that a switching frequency of 7.5 kHz is more energy efficient at lower RPM:s, whereas for higher RPM:s it is more efficient to use higher switching frequencies of 10 to 12.5 kHz. It can be concluded that having a varying switching frequency is beneficial in terms of total EDU power efficiency. It also shows that there is a trade-off situation regarding the losses in the inverter versus the losses in the electrical machine. Higher switching frequencies gives increased inverter losses but the losses in the IPMSM decrease.

By comparing the modulation principles the conclusion drawn is that SVPWM brings total less losses compared to the DPWM principle in the entire drive system for all examined OP:s and switching frequencies. DPWM is more power efficient for high switching frequencies in the inverter but has larger losses in the electrical machine.

The results from the simulation has a mean difference of 3.5 %-points from the physical tests, with an error that increases with switching frequency and an offset dependent on torque. Due to the lack of precise loss data in the physical tests it cannot be further concluded on which parts of the model that yields this difference.

7
Ethics & Sustainability

The main focus of this thesis work has been to examine and further develop the power efficiency of EV:s. While there are many positive aspects of EV:s, such as low to zero emission of both pollution and noise, there are also some negative aspects in regard of ethics and sustainability.

The production of the high duty batteries needed is as of today not very environmentally friendly. The batteries usually consists of minerals such as lithium, nickel and cobalt whose mining process can lead to water pollution and habitat destruction for local wildlife and communities [33]. There are also numerous reports of bad working conditions and the exploitation of child labour in the mines where these minerals are gathered. Similar concerns exists in gathering the materials for the permanent magnets used in the electrical machine. A transparent supply chain where all steps are scrutinized is crucial for a fair production.

Additionally, the proper disposal of these batteries when they have reached their end of life is a costly process in terms of money and energy [34]. Due to this, the problem of toxic waste and insufficient recycling of these minerals exists as well and is something that would be beneficial to further develop.

Comparing the complete life cycle analysis between a traditional Internal Combustion Engine Vehicle (ICEV) to that of an EV, the EV generally has less total greenhouse gas emission than the ICEV [35]. This holds if the EV:s battery is recycled properly, another important part is how the electricity used to charge the EV is generated. Using fossil free sources of electricity is a key part of reducing emissions and greatly affects the total emission of the EV.

Bibliography

[1] R. Menon, N. A. Azeez, A. H. Kadam, and S. S. Williamson, "Energy loss analysis of traction inverter drive for different pwm techniques and drive cycles," in *2018 IEEE International Conference on Industrial Electronics for Sustainable Energy Systems (IESES)*, 2018, pp. 201–205.

[2] D. Cittanti, V. Mallemaci, F. Mandrile, S. Rubino, R. Bojoi, and A. Boglietti, "Pwm-induced losses in electrical machines: An impedance-based estimation method," in *2021 24th International Conference on Electrical Machines and Systems (ICEMS)*, 2021, pp. 548–553.

[3] L. S.A., B. S. Rajpourhit, and A. Jain, "Modeling and analysis of 3-phase vsi using spwm technique for grid connected solar pv system," in *2014 IEEE Students' Conference on Electrical, Electronics and Computer Science*, 2014, pp. 1–6.

[4] S. N. Vukosavic, *Grid-Side Converters Control and Design*, 1st ed. Belgrade: Springer Cham, 2018.

[5] S. Shen and Q.-z. Chen, *Inverter PWM Control*. Cham: Springer International Publishing, 2024, pp. 289–318. [Online]. Available: https://doi.org/10.1007/978-3-031-38161-4_9

[6] F. Sevilmiş and H. Karaca, "Simulation and analysis of svpwm based vsi for wind energy systems," in *Proceedings of the 2014 6th International Conference on Electronics, Computers and Artificial Intelligence (ECAI)*, 2014, pp. 73–78.

[7] L. Yan, X. Li, H. Hu, and B. Zhang, "Research on svpwm inverter technology in wind power generation system," in *2011 International Conference on Electrical and Control Engineering*, 2011, pp. 1220–1223.

[8] A. Hava, R. Kerkman, and T. Lipo, "A high-performance generalized discontinuous pwm algorithm," *IEEE Transactions on Industry Applications*, vol. 34, no. 5, pp. 1059–1071, 1998.

[9] D. Graovac, M. Pürschel, and A. Kiep, *MOSFET Power Losses Calculation Using the Data-Sheet Parameters*, Infineon Technologies AG, 7 2006, infineon application note 1:1.

[10] S. Amirpour, T. Thiringer, and D. Hagstedt, "Power loss analysis in a sic/igbt propulsion inverter including blanking time, mosfet's reverse conduction and the effect of thermal feedback using a pmsm model," in *IECON 2020 The 46th Annual Conference of the IEEE Industrial Electronics Society*, 2020, pp. 1424–1430.

[11] W. Tong, *Motor Design Characteristics*. CRC Press, 2014. [Online]. Available: https://doi.org/10.1201/b16863

[12] Z. Cao, A. Mahmoudi, S. Kahourzade, and W. L. Soong, "An overview of electric motors for electric vehicles," in *2021 31st Australasian Universities Power Engineering Conference (AUPEC)*, 2021, pp. 1–6.

[13] C. Liu, K. T. Chau, C. H. T. Lee, and Z. Song, "A critical review of advanced electric machines and control strategies for electric vehicles," *Proceedings of the IEEE*, vol. 109, no. 6, pp. 1004–1028, 2021.

[14] A. Abdul and A. Altahir, "Park and clark transformations park and clark transformations: A short review," 04 2020.

[15] I. Qureshi and V. Sharma, "Wide speed range and torque control of ipmsm with mtpa-mtpv field weakening control," *Arabian Journal for Science and Engineering*, 12 2023.

[16] W. H. Hayt, *Engineering Electromagnetics*, 5th ed. New York: McGraw-Hill, 1989.

[17] Y. Liu, J. Tang, N. Sharma, and A. Rodionov, *Electrical machines, design and analysis*. unpublished.

[18] P. Osekar, S. Kalligudd, S. Angadi, and A. B. Raju, "Field oriented control of surface-mount pmsm using model predictive current control," in *2022 IEEE North Karnataka Subsection Flagship International Conference (NKCon)*, 2022, pp. 1–5.

[19] S. bai and E. wei Zhang, "Based on the model of the dq axis permanent magnet synchronous motor mpc," in *Proceedings of 2011 International Conference on Electronics and Optoelectronics*, vol. 3, 2011, pp. V3–224–V3–226.

[20] M. Zordan, P. Vas, M. Rashed, S. Bolognani, and M. Zigliotto, "Field-weakening in high-performance pmsm drives: a comparative analysis," in *Conference Record of the 2000 IEEE Industry Applications Conference. Thirty-Fifth IAS Annual Meeting and World Conference on Industrial Applications of Electrical Energy (Cat. No.00CH37129)*, vol. 3, 2000, pp. 1718–1724 vol.3.

[21] H. Chaoui, M. Khayamy, and O. Okoye, "Mtpa based operation point speed tracking for pmsm drives without explicit current regulation," *Electric Power Systems Research*, vol. 151, pp. 125–135, 2017. [Online]. Available: https://www.sciencedirect.com/science/article/pii/S0378779617302080

[22] V. T. Ha and P. T. Giang, "Field—weakening control with maximum torque per ampere (mtpa) for electric vehicle (ev) application," in *Computational Intelligence Methods for Green Technology and Sustainable Development*, Y.-P. Huang, W.-J. Wang, H. A. Quoc, H.-G. Le, and H.-N. Quach, Eds. Cham: Springer International Publishing, 2023, pp. 531–541.

[23] M. Fadel, L. Sepulchre, and M. Pietrzak-David, "Deep flux-weakening strategy with mtpv for high-speed ipmsm for vehicle application," *IFAC-PapersOnLine*, vol. 51, no. 28, pp. 616–621, 2018, 10th IFAC Symposium on Control of Power and Energy Systems CPES 2018. [Online]. Available: https://www.sciencedirect.com/science/article/pii/S2405896318334931

[24] Y. Liang, F. Zhao, K. Xu, W. Wang, J. Liu, and P. Yang, "Analysis of copper loss of permanent magnet synchronous motor with formed transposition winding," *IEEE Access*, vol. 9, pp. 101 105–101 114, 2021.

[25] A. Bardalai, D. Gerada, Z. Xu, and C. Gerada, "Ac loss analysis in winding of electrical machines with varying strands-in-hand and bundle shapes," in *2020*

23rd International Conference on Electrical Machines and Systems (ICEMS), 2020, pp. 845–850.

[26] E. Roshandel, A. Mahmoudi, S. Kahourzade, and W. L. Soong, "Efficiency maps of electrical machines: A tutorial review," *IEEE Transactions on Industry Applications*, vol. 59, no. 2, pp. 1263–1272, 2023.

[27] T. Velic, M. Barkow, D. Bauer, P. Fuchs, J. Wende, T. Hubert, M. Reinlein, J. Nägelkrämer, and N. Parspour, "Efficiency optimization of electric drives with full variable switching frequency and optimal modulation methods," in *2021 17th Conference on Electrical Machines, Drives and Power Systems (ELMA)*, 2021, pp. 1–6.

[28] X. Lv, D. Sun, and L. Sun, "Determination of iron loss coefficients of ferromagnetic materials used in cryogenic motors," in *2019 22nd International Conference on Electrical Machines and Systems (ICEMS)*, 2019, pp. 1–5.

[29] "Bibliography," in *Transformers and Motors*, G. P. Shultz, Ed. Boston: Newnes, 1989, pp. 311–312. [Online]. Available: https://www.sciencedirect.com/science/article/pii/B9780080519586500184

[30] Z.-Q. Zhu, S. Xue, W. Chu, J. Feng, S. Guo, Z. Chen, and J. Peng, "Evaluation of iron loss models in electrical machines," *IEEE Transactions on Industry Applications*, vol. 55, no. 2, pp. 1461–1472, 2019.

[31] K. Okamoto, "Chapter 6 - finite element method," in *Fundamentals of Optical Waveguides (Third Edition)*, third edition ed., K. Okamoto, Ed. Academic Press, 2022, pp. 271–338. [Online]. Available: https://www.sciencedirect.com/science/article/pii/B9780128156018500069

[32] *CAB450M12XM3, Datasheet*, Wolfspeed, 2024, rev. 2. [Online]. Available: https://www.wolfspeed.com/products/power/sic-power-modules/xm3-power-module-family/cab450m12xm3/

[33] F. M. et al., "Climate change 2014: Mitigation of climate change. contribution of working group iii to the fifth assessment report of the intergovernmental panel on climate change," in *Industry*, R. Clift, Ed. Cambridge, United Kingdom: Cambridge University Press, 2014, pp. 311–312. [Online]. Available: https://www.ipcc.ch/site/assets/uploads/2018/02/ipcc_wg3_ar5_chapter10.pdf

[34] B. Miloradović, E. M. Bigorra, T. Nolte, and A. V. Papadopoulos, "Challenges in the automated disassembly process of electric vehicle battery packs," in *2023 IEEE 28th International Conference on Emerging Technologies and Factory Automation (ETFA)*, 2023, pp. 1–4.

[35] R. Nealer and T. Hendrickson, "Review of recent lifecycle assessments of energy and greenhouse gas emissions for electric vehicles," *Current Sustainable/Renewable Energy Reports*, vol. 2, 07 2015.

DEPARTMENT OF ELECTRICAL ENGINEERING
CHALMERS UNIVERSITY OF TECHNOLOGY
Gothenburg, Sweden
www.chalmers.se

CHALMERS
UNIVERSITY OF TECHNOLOGY